Key Points:
- Numerical model, combining viscoelastoplasticity, rate and state friction, and elastodynamics, simulates the growth of strike-slip faults
- Two distinct fault growth modes, seismic and aseismic, can be distinguished by their fault orientation relative to regional stresses
- The model explains altered stress orientations during the genesis of the Landers-Mojave fault system

Correspondence to:
S. Preuss,
sipreuss@ethz.ch

Seismic and Aseismic Fault Growth Lead to Different Fault Orientations

Simon Preuss[1] ![ID], **Robert Herrendörfer[1,2]** ![ID], **Taras Gerya[1]** ![ID], **Jean-Paul Ampuero[3]** ![ID], **and Ylona van Dinther[2,4]** ![ID]

[1]Geophysical Fluid Dynamics, Institute of Geophysics, Department of Earth sciences, ETH Zürich, Zürich, Switzerland, [2]Seismology and Wave Physics, Institute of Geophysics, Department of Earth sciences, ETH Zürich, Zürich, Switzerland, [3]Géoazur Laboratory, Institut de Recherche pour le Développement-Université Côte d'Azur, Campus Azur du CNRS, Valbonne, France, [4]Tectonics, Department of Earth Sciences, Utrecht University, Utrecht, The Netherlands

Abstract Orientations of natural fault systems are subject to large variations. They often contradict classical Coulomb failure theory as they are misoriented relative to the regional Andersonian stress field. This is ascribed to local effects of structural or stress heterogeneities and reorientations of structures or stresses on the long term. To better understand the relation between fault orientation and regional stresses, we simulate spontaneous fault growth and its effect on the stress field. Our approach incorporates earthquake rupture dynamics, viscoelastoplastic brittle deformation and a rate- and state-dependent friction formulation in a continuum mechanics framework. We investigate how strike-slip faults orient according to local and far-field stresses during their growth. We identify two modes of fault growth, seismic and aseismic, distinguished by different fault angles and slip velocities. Seismic fault growth causes a significant elevation of dynamic stresses and friction values ahead of the propagating fault tip. These elevated quantities result in a greater strike angle relative to the maximum principal regional stress than that of a fault segment formed aseismically. When compared to the near-tip time-dependent stress field the fault orientations produced by both growth modes follow the classical failure theory. We demonstrate how the two types of fault growth may be distinguished in natural faults by comparing their angles relative to the original regional maximum principal stress. A stress field analysis of the Landers-Kickapoo fault suggests that an angle greater than ~25° between two faults indicates seismic fault growth.

1. Introduction

Strike-slip faults that are hundreds of kilometers long formed from smaller defects (e.g., Hirsch, 1975; Regenauer-Lieb & Yuen, 2003; Regenauer-Lieb et al., 2006) and grow larger as they accommodate more strain (e.g., Nur et al., 1993; Perrin, Manighetti, Gaudemer, et al., 2016, Perrin, Manighetti, Ampuero, et al., 2016). As a result, faults are large complex zones of fractured rock and slip surfaces that are inherently composite. Commonly, these structures are approximated as two-dimensional slip surfaces. The classical understanding of fault growth relates fault length linearly to accumulated displacement due to episodically recurring earthquakes (e.g., Bürgmann et al., 1994; Cowie & Scholz, 1992b; 1992a; Manighetti et al., 2001, 2004; Norris & Toy, 2014; Perrin, Manighetti, Gaudemer, et al., 2016, Perrin, Manighetti, Ampuero, et al., 2016; Peacock, 1991; Peacock & Sanderson, 1996; Scholz & Lawler, 2004; Segall & Pollard, 1983). A gradual extension in fault length increases the fault surface area, which augments its potential to generate bigger earthquakes. Since strike-slip faults typically consist of a vertical or subvertical dipping fault plane as described first by Anderson (1905), the degrees of freedom during fault lengthening reduce to one parameter, the horizontal fault angle. The angle of upper crustal faults is widely believed to obey the Mohr-Coulomb failure criterion (Norris & Toy, 2014; Sibson, 1994; Sibson et al., 2011) as set out by Anderson (1942) and Byerlee (1978). This criterion is a standard rule of thumb in assessing optimally oriented faults (Fang & Dunham, 2013) and it is largely validated by the WorldStressMapProject (Heidbach et al., 2018). The angle α between a newly forming, mechanically stable fault and the maximum principal compressional stress direction σ_1 was shown to follow one of the three types (e.g., Arthur et al., 1977; Choi & Petersen, 2015; Kaus, 2010; Vermeer, 1990; Zang & Stephansson, 2010, p. 39):

Roscoe angle:

$$\alpha_{R_{1-4}} = \pm \left(\frac{\pi}{4} \mp \frac{\psi}{2} \right), \tag{1}$$

Coulomb angle:

$$\alpha_{C_{1-4}} = \pm \left(\frac{\pi}{4} \mp \frac{\varphi}{2} \right),$$
(2)

Arthur angle:

$$\alpha_{A_{1-4}} = \pm \left(\frac{\pi}{4} \mp \frac{\varphi + \psi}{4} \right),$$
(3)

where ψ is the dilation angle that represents volumetric change in shear deformations and φ is the internal angle of friction, related to μ, the friction coefficient, as $\mu = \tan\varphi$. The Roscoe and Coulomb angles are upper and lower bounds, and the Arthur angle is defined as the mean of these two angles (Arthur et al., 1977). Despite the general agreement on these failure criteria, many natural faults deviate substantially from their predictions (Anderson, 1905; Fletcher et al., 2016; Hardebeck & Michael, 2004; Perrin, Manighetti, Gaudemer, et al., 2016; Scholz et al., 2010; Sibson, 1990; Sibson et al., 2011; Townend & Zoback, 2004). One reason for this discrepancy might be a long-term rotation of the stress field surrounding the fault. This is caused by an adaptation to changing tectonic conditions, although the fault most likely formed in accordance with the stress state prevailing at the time of genesis of the structure (Zang & Stephansson, 2010, p. 247).

However, the stress field can additionally undergo short-term changes: Elastodynamic singular crack and nonsingular slip-weakening models have shown that the dynamic stress field near the tip of a propagating rupture depends on the dynamics of this rupture (Andrews, 1976; Erdogan, 1968; Fossum & Freund, 1975; Freund, 1972a, 1972b; Kame et al., 2003; Poliakov et al., 2002; Rice, 1980) and instantaneous fault slip causes an alteration of the stress field around the fault (Segall & Pollard, 1980). This suggests, in the first place, that the stress field might rotate not only due to long-term stress reorientations as argued above but also due to short-term *dynamic* effects. Second, and equally important, this suggests that *near-fault* and remote stress field might deviate during dynamic earthquake rupture. Such changes to the stress and strain around the fault were, for example, predicted by applying a maximum strain energy density criterion, however, without capturing dynamic stress field changes as fault slip evolves nor capturing changes to the coefficient of friction (Du & Aydin, 1995). The well-established rock friction experiments of Dieterich and Ruina demonstrated the clear dependency of the friction coefficient on the slip velocity (Dieterich, 1979, 1981; Ruina, 1983). Taken together, the above findings lead to our first hypothesis: The local instantaneous near-tip stress field and the time-, velocity-, and state-dependent local friction coefficient control the angle of incipient and growing faults. Thus, to assess fault angles correctly, these time- and space-dependent quantities need to be considered. This proposition is in contrast to the practice of applying usually available far-field or postformation quantities. We hypothesize that during aseismic fault growth far-field and local stress orientations deviate insignificantly, while during dynamic (seismic) fault growth the near-field stresses do deviate significantly from the remote ones. We note that aseismic fault growth driven by aseismic creep could be approximated by a static modeling assumption.

Fracture mechanics predicts that both aseismic and seismic fault slip produce stress concentrations at a fault's edges. These elevated stresses promote spontaneous crack growth and, thus, dynamics may alter the crack or shear band growth direction (Kame & Yamashita, 2003, 1999; Kame et al., 2003). For example, Ma and Elbanna (2018) showed that the localization pattern depends on the inertia effect. Indeed, fault growth partly occurs dynamically during earthquakes (e.g., Andrews, 2005; Manighetti et al., 2005; Perrin, Manighetti, Ampuero, et al., 2016; Schaff & Beroza, 2004). The other part of fault growth might be driven by static stress concentration near growing fault tips (e.g., Aydin & Berryman, 2010; Cooke, 1997; Lehner et al., 1981; Perrin, Manighetti, Ampuero, et al., 2016; Willemse & Pollard, 1998). The results are slowly moving disturbances of aseismic deformation (Ida, 1974) indicating that fault creep is kinematically similar to seismic faulting and may be sizable in tectonic strain release (King et al., 1973). This leads to our second hypothesis: Similarly to the existence of different modes of fault slip, different modes of fault growth may exist; we propose two end member cases that happen on earthquake and geological timescales: seismic versus aseismic growth. It is however challenging to distinguish by field observations if growth was seismic or aseismic.

Despite multidisciplinary efforts to study factors that control fault angles, no concept that differentiates between modes of fault growth has been established. One reason is that tackling this problem in a computational study requires a combination of challenging ingredients: (i) self consistent long-term stress buildup

that allows for a realistic fault zone setting due to spontaneous fault growth; (ii) dynamic pressure; (iii) earthquake dynamics; (iv) adaptive time stepping due to the large difference in timescales (hundreds of years for fault evolution to milliseconds for rupture events); (v) a laboratory-based friction formulation (Dieterich, 1979, 1981; Ruina, 1983); (vi) (visco)elastoplastic rheology.

The recently developed seismo-thermomechanical modeling framework (van Dinther, Gerya, Dalguer, Mai, et al., 2013, van Dinther, Gerya, Dalguer, Corbi, et al., 2013) with adaptive time stepping and an invariant continuum-based rate- and state-dependent friction formulation (STM-RSF) offers the full combined spectrum of the needed ingredients (Herrendörfer et al., 2018). This 2-D STM-RSF code is in line with the geodynamic modeling approach as it allows for large deformation simulations of self-consistently evolving fault zones on geological timescales (Gerya & Yuen, 2007; van Dinther et al., 2014). STM-RSF additionally resolves all stages of an earthquake cycle with realistic rupture properties in a viscoelastoplastic compressible continuum that allows for fault growth along spontaneous rupture paths. The code simulates fault slip events at seismic slip rates and rupture speeds at which shear and pressure waves are generated.

By using this STM-RSF modeling framework we for the first time identify two distinctly different modes of fault growth, seismic and aseismic, which occur on substantially different timescales. Our study shows that both modes can be distinguished by knowing only few measurable quantities: fault angle, remote maximum principal stress orientation, and static friction coefficient of the host rock. Our presented results are insensitive to physical parameter changes and converge with numerical grid size. The applied methodology can help in assessing whether a fault formed seismically or aseismically. Furthermore we give an explanation for the typically observed fault bends in strike-slip faults and shed light on general aspects of fault growth

2. Methods

We present the main ingredients of the applied STM-RSF modeling approach (Herrendörfer et al., 2018) in section 2.1. We introduce the model setup and parameters in section 2.2.

2.1. STM-RSF

The 2-D problem we solve for is the conservation of mass:

$$\rho \frac{\partial v_i}{\partial x_i} = -\frac{D\rho}{Dt}, \tag{4}$$

and the conservation of momentum:

$$\frac{\partial \tau_{ij}}{\partial x_j} - \frac{\partial P}{\partial x_i} = \rho \frac{\mathrm{D}v_i}{\mathrm{D}t} - \rho g_i, \tag{5}$$

where ρ denotes density, $\frac{\mathrm{D}}{\mathrm{D}t}$ is the material time derivative, i and j are coordinate indices, x_i and x_j represent spatial coordinates, v_i is velocity, P is the dynamic pressure, g_i is gravity, and τ_{ij} denotes the deviatoric stress tensor given as

$$\tau_{ij} = \sigma_{ij} + \delta_{ij}P, \tag{6}$$

with σ_{ij} being the Cauchy stress tensor and δ_{ij} being the Kronecker delta. Dynamic pressure P is given by the mean stress:

$$P = -\frac{\sigma_{kk}}{3}, \qquad \text{with} \quad k = 1, 2, 3, \tag{7}$$

where P is positive under compression. Computing the dynamic pressure as a solution of the continuity and momentum equations is especially crucial to obtain correct angles of forming faults that differ from a constant Roscoe angle (Buiter, 2012; Buiter et al., 2016; Kaus, 2010). Because our simulation represents a compressive state of stress, that is, $\sigma_1 > \sigma_2$ and we ignore dilation, that is, $\psi=0$, the four potential fracture surface orientations predicted by the Arthur angle (equation (3)) reduce to $\alpha_1 = 45° -(\varphi/4)$ and $\alpha_2 = -45° +(\varphi/4)$ (conjugate). Thus, the second pair of tensile fracture angles extinguishes. We assume a compressible medium with a compressibility defined via the bulk modulus K as

$$\frac{\mathrm{D}\rho}{\mathrm{D}t} = \frac{\rho}{K} \frac{\mathrm{D}P}{\mathrm{D}t}. \tag{8}$$

This material is furthermore restricted to a viscoelastoplastic rheology, in which, due to the choice of the initial viscosity value, the material essentially behaves as elastoplastic (section 2.2). Damage representing the reduction of elastic moduli during deformation is neglected for reasons of simplicity. A constitutive relationship, which links deviatoric stresses τ_{ij} and deviatoric strain rates $\dot{\varepsilon}'_{ij}$, is adopted according to Gerya and Yuen (2007):

$$\dot{\varepsilon}'_{ij} = \frac{1}{2G}\frac{\overset{\triangledown}{D}\tau_{ij}}{Dt} + \frac{1}{2\eta}\tau_{ij} + \dot{\varepsilon}'_{II(\text{plastic})}\frac{\tau_{ij}}{\tau_{II}},\tag{9}$$

where G is the shear modulus, $\frac{\overset{\triangledown}{D}}{Dt}$ denotes the corotational time derivative, η is the effective ductile viscosity, $\dot{\varepsilon}'_{II\,(\text{plastic})}$ is the second invariant of the deviatoric plastic strain rate and $\tau_{II} = \sqrt{\tau_{xx}^2 + \tau_{xy}^2}$ is the second invariant of the deviatoric stress tensor. We use the yield function F to define the onset of plastic deformation by the yield criterion $F = 0$. The yield function is governed by a Drucker-Prager (Drucker & Prager, 1952) plastic yield function:

$$F = \tau_{II} - \sigma_{\text{yield}}, \quad \sigma_{\text{yield}} = \mu_l(1-\lambda)P + C,\tag{10}$$

where μ_l is the local friction coefficient, C denotes cohesion (residual shear strength), λ is the pore fluid pressure factor, and σ_{yield} is the pressure-dependent scalar material yield strength. The invariant quantities μ_l, P, τ_{II}, and σ_{yield} are scalars that are independent of the coordinate system and can vary both in space and time. As local stresses are increased toward the yield criterion, plastic strain rates become noticeable once the local strength of the material is overcome (Herrendörfer et al., 2018; Nakatani, 2001) and plastic deformation slowly starts to localize. In our continuum mechanics approach fault slip is represented by plastic strain occurring in a shear band or fault zone of finite width, which can occur at every marker. Brittle creep experiments showed that inelastic strain is an appropriate proxy for the microstructural state of a rock, which corresponds primarily to the growth of dilatant microcracks between or inside the grains (Brantut et al., 2014). Further, an empirically derived relation between strain rate and stress difference for intact materials can be seen as analogous to the rate-and-state law for frictional sliding along preexisting interfaces, because chemically activated subcritical crack growth processes, such as stress corrosion reactions, have an activation volume very similar to that of thermally activated processes in rate-and-state friction (Brantut et al., 2014). Furthermore, a rate-and-state-dependent plastic bulk model has been proposed to control bulk yield stress using damage/temperature as state variables (Roubíček, 2014). To study the evolution and growth of a seismically active fault zone we adopt a continuum-based invariant formulation of rate-and-state friction for the first time. This approach is in contrast to classical seismic cycle simulations (e.g., Liu & Rice, 2007; Lapusta & Liu, 2009; Lapusta et al., 2000; Rice, 1993), in which fault strength is evaluated using normal stress σ_n and shear stress τ_s on a predefined fault. By prescribing a weak perturbation in the center of the model (section 2.2) we prescribe the location of fault initiation and prevent fault nucleation at other points. We assume $C = 0$ MPa, as typically done in rate- and state-dependent friction modeling. This choice is explained in section 4.5. We further assume that $\sigma_{\text{yield}} = \tau_{II}$ and thus, $F = 0$. The invariant reformulation of the classical rate- and state-dependent friction formalism according to Herrendörfer et al. (2018) reads as

$$\tau_{II} = \sigma_{\text{yield}} = \mu_l(1-\lambda)P = a \quad P \quad \text{arcsinh}\left[\frac{V_p}{2V_0}\exp\left(\frac{\mu_0 + b\ln\frac{\theta V_0}{L}}{a}\right)\right](1-\lambda),\tag{11}$$

where a and b are laboratory-based, empirical rate- and state-dependent friction values, L is the rate- and state-dependent friction characteristic slip distance, and V_0 is an arbitrary reference slip velocity (Lapusta & Barbot, 2012). The parameter μ_0 is the reference static friction coefficient, θ denotes the evolving state variable with the aging evolution law

$$\frac{d\theta}{dt} = 1 - \frac{V_p\theta}{L},\tag{12}$$

and V_p is the plastic slip rate defined by
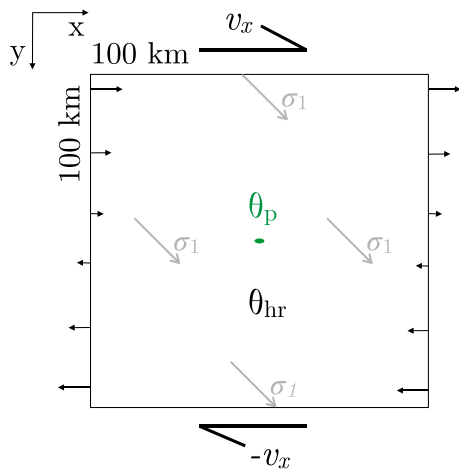
$$V_p = 2\dot{\varepsilon}'_{II(p)}W,\tag{13}$$

Figure 1. Model setup of the dextral inplane strike-slip simulation. Box of size 100 km × 100 km with 401 × 401 nodes in x and y direction, respectively (grid resolution of 250 m). Bold black arrows show direction of Dirichlet v_x-velocity boundary conditions applied in opposite direction: $v_x = \pm 1.0 \cdot 10^{-9}$ m/s = ±3.15 cm/year. At left and right boundaries Neumann boundary conditions for v_x are prescribed. The vertical velocity v_y is set to zero at all boundaries. The initial state θ_p is perturbed in an area of an elliptical shape (green) of twice the grid step size in x direction ($2\Delta x$), by setting it ∼403 times lower compared to that in the surrounding host rock. Gray arrow marks direction of initial σ_1 direction.

where W denotes the thickness or width of the fault zone in the continuous host rock. Following van Dinther, Gerya, Dalguer, Mai, et al. (2013) and Herrendörfer et al. (2018) we define $W = \Delta x$, where Δx is the numerical grid size. We use this approximation because in classical applications of plasticity the deformation localizes to within 1–2 grid cells (e.g., Lavier et al., 2000; van Dinther, Gerya, Dalguer, Corbi, et al., 2013). However, this formulation makes the problem grid size dependent. We demonstrate in section 3.4 that this grid size dependence does not impact our conclusions. The relationship between slip rate and plastic strain rate may need a physics-based redefinition if deformation is distributed within more than a grid cell during the localization process toward a mature fault zone. This problem will be addressed in a future study in detail (section 4.3).

To solve the governing equations, we use a 2-D numerical technique with an implicit, conservative finite-differences scheme on a fully staggered grid combined with the marker-in-cell technique (Gerya & Yuen, 2003, 2007). All details of the numerical technique that comprise the STM-RSF code can be found in Herrendörfer et al. (2018).

2.2. Model Setup

The model setup represents a generic case to study the evolution of a fault zone. It is a 2-D plane strain model, in which the fault zone propagates as a mode II crack. The initial experimental geometry, together with the Dirichlet v_x-velocity boundary conditions applied in opposite directions at the top and bottom boundaries, represents a dextral strike-slip zone (Figure 1).

In such a dextral shear experiment the maximum compressive stress σ_1 is initially oriented at an angle of 45° to the imposed shear direction (e.g., Meyer et al., 2017), indicated by the gray arrow in Figure 1. We apply a weak perturbation in the center of the model, which will be the locus of stress concentration and thus the starting point of spontaneous fault growth. Rate- and state-dependent friction and material parameters were adopted from Herrendörfer et al. (2018). Values for these parameters (Table 1) are largely in accordance with Lapusta et al. (2000) with differences in the choice of V_0, μ_0, and the initial mean stress P_B. V_0 is interpreted as loading slip rate. Combination of elevated fluid pressure, found in a wide area surrounding fault zones (Hardebeck & Hauksson, 1999),

Table 1
Rate- and State-Dependent Friction and Material Parameters

| Parameter	Symbol	Value
Shear modulus	G	30 GPa
Bulk modulus	K	50 GPa
Density	ρ	2,700 kg/m^3
Shear wave speed	c_s	3.3 km/s
Effective viscosity	η	$5 \cdot 10^{26}$ Pa s
Initial mean stress (pressure)	P_B	5 MPa
Gravity	g_i	0 m/s^2
Reference static friction coefficient	μ_0	0.2
Reference slip velocity	V_0	$2 \cdot 10^{-9}$ m/s = 6.3 cm/year
Characteristic slip distance	L	0.0075 m
Rate- and state-dependent friction direct effect	a	0.011
Rate- and state-dependent friction evolution effect	b	0.018
Initial state		
Host rock	θ_{hr}	$\frac{L}{V_0} \exp(5)$ s ≈ 17.64 years
Perturbation	θ_p	$\frac{L}{V_0} \exp(-1)$ s ≈ 0.04 years
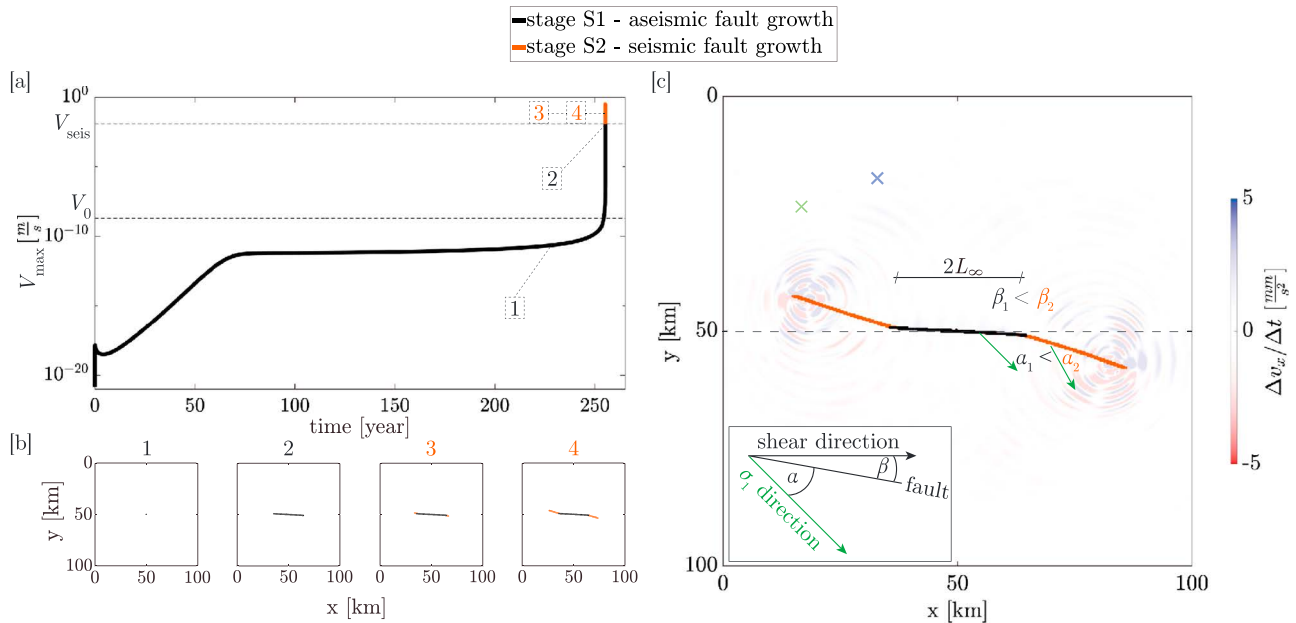
Figure 2. Two stages of fault growth with distinctly different slip velocities. The two faulting stages are indicated by color. (a) Maximum slip velocity versus time in years. V_0 and V_{seis} are indicated. V_{seis} is the threshold slip velocity that separates seismic and aseismic faulting stages. Numbers indicate the substages of fault evolution shown in the snapshots in (b). (b) Four numbered snapshots of plastic strain ($\varepsilon_p > 10^{-4}$). (c) Modeled fault pattern indicated by plastic strain ($\varepsilon_p > 10^{-4}$) at the end of the simulation overlain with seismic waves indicated by horizontal acceleration at this instant. L_∞ indicates the theoretical nucleation length, α is the angle between the two fault segments and the σ_1-direction (green arrow in the inset), $\alpha_1 < \alpha_2$. β is the angle between the horizontal E-W shearing direction (0°, black dashed line) and the respective fault segment, $\beta_1 < \beta_2$. Green and blue crosses mark accelerometer locations for seismogram in Figure 10.

and mean low permeability in the crust (Manning & Ingebritsen, 1999) result in fluid overpressuring above hydrostatic values ($\lambda > 0.4$) and approaching lithostatic values ($\lambda \sim 1.0$) (Sibson & Rowland, 2003), which reduces the effective lithostatic pressure and as a consequence reduces the frictional sliding resistance of the crustal material. This agrees with the notion that water during sliding experiments decreases the coefficient of friction (Kohlstedt et al., 1995). Hence, we choose $\lambda \sim 0.67$ and a lower static friction coefficient of $\mu_0 = 0.2$ with respect to Byerlee friction of 0.6. The initial pressure $P_B = 5$ MPa is an effective quantity that is lowered due to pore fluid pressure P_f and is related to the initial lithostatic pressure $P_{B_{lith}}$ as

$$P_B = (P_{B_{lith}} - P_f) = P_{B_{lith}}(1 - \lambda). \tag{14}$$

Thus, $P_{B_{lith}} = 15.2$ MPa, which is equivalent to a depth of 572 m, representing the upper crust. To confirm that our conclusions concerning fault angles hold true across upper crustal depths, we investigate the role of μ_0 and P_B in section 3.5.

Note that Newtonian viscosity is constant and linear during these simulations which, for simplicity, ignore any nonlinear effects of temperature and strain rate on the viscous rheology typically adopted in geodynamic models (van Dinther, Gerya, Dalguer, Mai, et al., 2013). The effective viscosity is set very high ($5 \cdot 10^{26}$ Pa s), which results in a mainly elastoplastic material behavior.

3. Results

In the reference model, we observe two successive stages of fault growth (stages S1 and S2) with slip velocities of distinctly different magnitudes (Figure 2). In the following we analyze these different stages in terms of fault angle, stress orientation, slip rate, and earthquake dynamics. For both faulting stages μ_l and σ_1 direction are systematically measured at the current position of the fault tip where slip velocity and local friction value have their momentary global maximum (Figure 4). To select the exact location of the fault tip we use a square that surrounds the current global maximum of the local friction value $\mu_{l_{max}}$ (green filled square in Figure 4) and sample the friction values that fulfill $\mu_l \geq \xi\mu_{l_{max}}$ with $\xi = 0.5, 0.95$, and 0.99. This sampling approach using different percentiles ξ allows for a shape-independent sample box picking. From the average data from the three percentiles we obtain the friction value μ_l^{av} at the fault tip. The σ_1 direction is averaged at the same points and thus referred to as σ_1^{av}. It is important to choose the size of the square
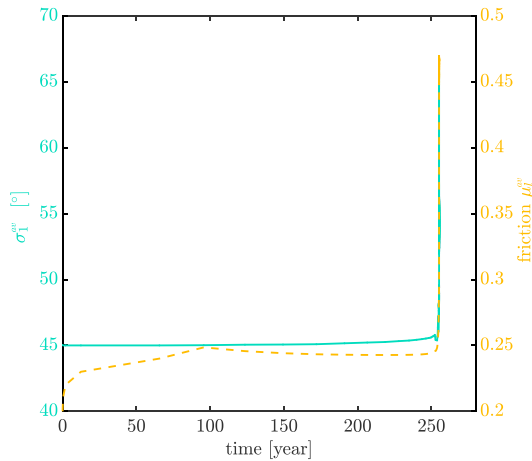
Figure 3. Maximum friction μ_l^{av} and σ_1^{av}, which are averaged in the area around the propagating fault tip versus time in years.

large enough to exclude outliers and small enough to avoid oversampling. A test with six different square sizes showed that a box of 1×1 km best captured the relevant short-wavelengths variations.

3.1. Stage 1: Aseismic Fault Growth

At the beginning of the first stage of faulting (S1), the entire model is elastically loaded due to the imposed shearing at the upper and lower boundaries. In the first 70 years stresses concentrate at the boundary of the weak perturbation. During this initial localization process, the logarithm of the global maximum slip velocity $\log(V_{max})$ increases linearly (Figure 2a). At the end of the localization process two new shear surfaces emerge and the growth rate of slip velocity decreases. One shear band with orientation close to the E-W oriented shear direction and one conjugate shear band (not shown) develop in the model center at the location of the weak perturbation. The E-W shear band is favored due to the elliptical shape of the weak perturbation and the imposed shear direction. This shear band starts to grow at both sides of the perturbation in $+x$ and $-x$ direction at an angle $\beta_1 = \pm 3.5°$ (Figures 2b and 4a). Since right and left shear b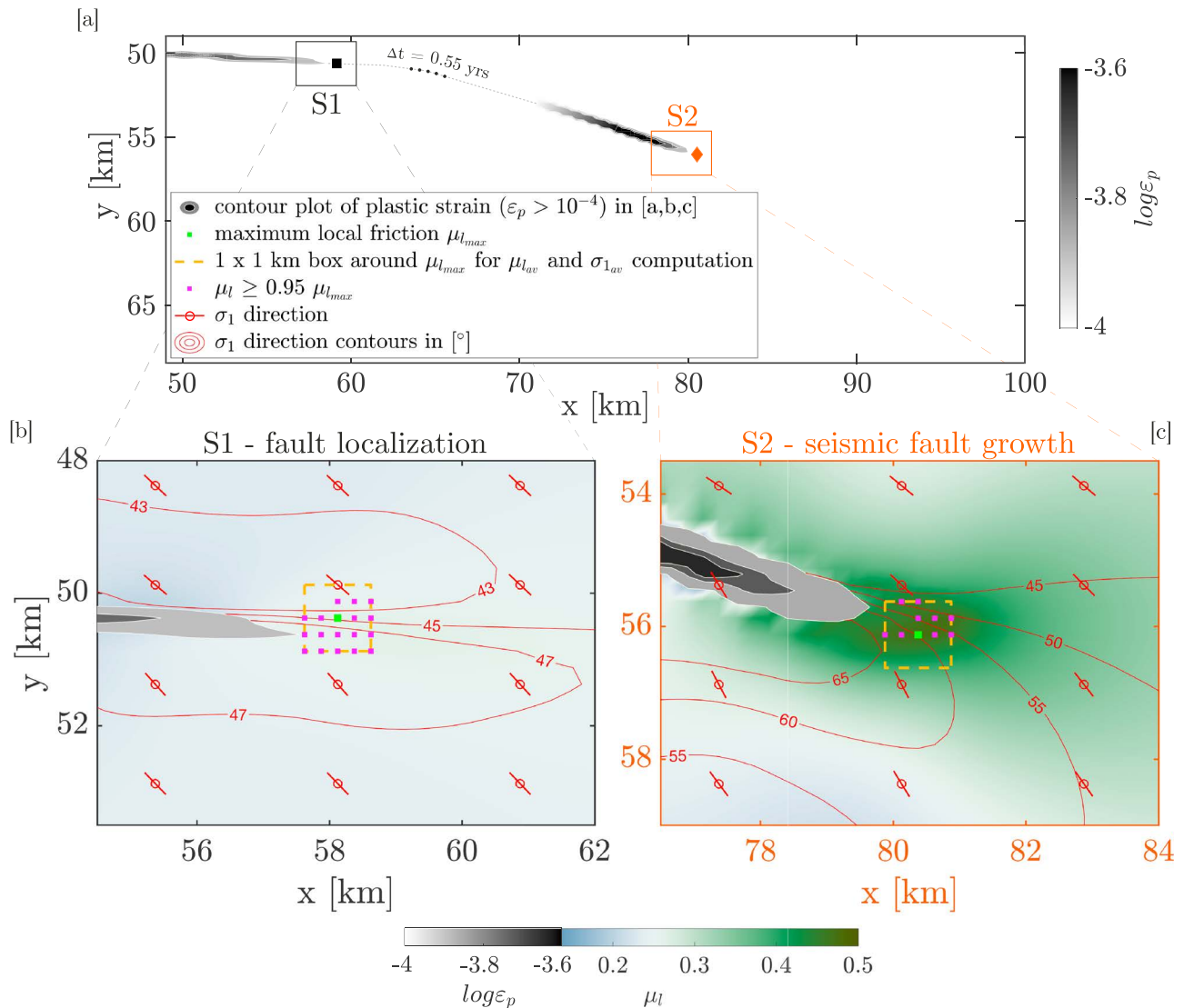ands grow in simultaneous and symmetric fashion, we focus on the right branch (i.e., positive x and y sector) in the following. This branch reaches a length of 7.8 km after 254.5 years, at which point V_{max} has approached the reference slip velocity V_0 at the propagating shear band tip (Figure 2a). Interestingly, while $V_{max} < V_0$, μ_l^{av} and the orientation of σ_1^{av} are relatively constant in the entire model domain and remain close to their initial values (Figure 3). Within the next 0.72 years, V_{max} increases 7 orders of magnitude while it is still in the aseismic range of slip velocities. The fault continues to grow at a constant angle β_1 in this aseismic fault growth stage. Simultaneously, the shear band localizes further to a one grid step wide feature that now represents a localized fault strand with μ_l^{av} and the orientation of σ_1^{av} starting to increase slightly (Figure 3). This is caused by the direct effect of the rate- and state-dependent friction formulation, which represents the immediate increase of friction and stresses to an increase in V_p. The observed elevated slip velocities thus lead to $\mu_l^{av} = 0.26$ and $\sigma_1^{av} = 45.4°$ at the fault tip (Figure 4b). Moreover, the σ_1 direction decreases north of the fault (counterclockwise rotation) and increases south of the fault (clockwise rotation). We note here that the increase of friction (at the fault tip) and the slight rotation of stresses (north and south of the fault) occurs only very close to the propagating fault (Figure 4b). Far from the fault, in the rest of the model domain, both quantities remain very close to their initial values. We define the angle α as the difference between the σ_1 direction and the fault angle β according to $\alpha = \sigma_1 - \beta$. Combining the averaged maximum local friction coefficient μ_l^{av}, the σ_1^{av} direction and β_1, we are able to plot the angular-frictional relation for stage S1. The result is consistent with the Arthur angle prediction (black square in Figure 5a), which, in general, is a good approximation of the fault angle α (Choi & Petersen, 2015). The end of stage S1 is reached as V_{max} transitions to seismic slip velocities $V_{seis} = 0.012$ m/s, which is determined by Rubin and Ampuero (2005) as the slip velocity at which the radiation of seismic waves produces stress changes on the fault comparable to those induced by the direct effect of rate- and state-dependent friction:

$$V_{seis} = \frac{2aPc_s}{G}. \tag{15}$$

At this point the right fault segment attains a length of 14.5 km and is straight with $\beta_1 = \pm 3.5°$, which means that the entire fault is 29-km long.

3.2. Stage 2: Seismic Fault Growth

After the aseismic fault growth stage, a dynamic slip event nucleates at the location of the initial weak seed and the fault produces an earthquake. The length of left and right fault segments when V_{seis} is exceeded agrees well with the theoretical estimate of the nucleation size L_∞ of 14 km, which depends on rate- and state-dependent friction and material parameters and normal stress as Rubin and Ampuero (2005). We adapt this formulation using P instead of normal stress as done in invariant rate- and state-dependent friction formalism and explained before equation (11):

Figure 4. Evolution of friction μ_l and σ_1 direction for faulting stages S1 and S2. (a) Contour plot showing plastic strain in gray colors with white contours at two distinct points in time. Plot is cropped to first quadrant of the model domain. Location where friction and stress directions are picked are indicated by black square (S1) and orange diamond (S2). The evolution in between these two points in time (duration of 0.55 years) is displayed schematically by a gray dashed line and black dots. Panels (b) and (c) are snapshot zooms of the friction distribution, representative for stages S1 and S2, respectively. The fault itself is plotted as plastic strain ε_p in gray colors with white contours. Red lines with circle indicate pointwise local direction of σ_1, red contour lines represent the distribution of σ_1 orientations. Rotation of the σ_1 direction in stage S2 is evident. Orange box (1 km × 1 km) contains the global maximum of the friction coefficient, $\mu_{l_{max}}$, in its center (green filled square). Magenta filled squares in this box mark the values that are used to compute μ_l^{av}(0.26 and 0.46 for S1 and S2, respectively) and σ_1^{av} (45.4° and 56.3° for S1 and S2, respectively) according to three different percentiles (explanation at beginning of section 3). The average of these three values of μ_l^{av} and σ_1^{av} are used and plotted in Figure 5a.

$$L_\infty = \frac{2}{\pi} \frac{GbL}{(b-a)^2 P(1-\nu)},$$ (16)

The factor 2 difference between the length of the entire fault and the theoretical L_∞ stems from the thickness of the fault that is ∼2 times the grid size Δx. This doubles the apparent L in our simulation. Because simultaneously to the nucleation of the dynamic event, V_{max} exceeds the seismic slip velocity threshold V_{seis} (Figure 2a), we refer to this dynamic phase as seismic fault growth stage (S2).

It takes ∼5 s from the nucleation of the event in the center until two rupture fronts reach the fault tips that were formed in stage S1. During this process, V_{max} increases approximately by a factor of 5 (from 0.012 to 0.058 m/s), which results in the generation of shear and pressure waves as shown in the video in the
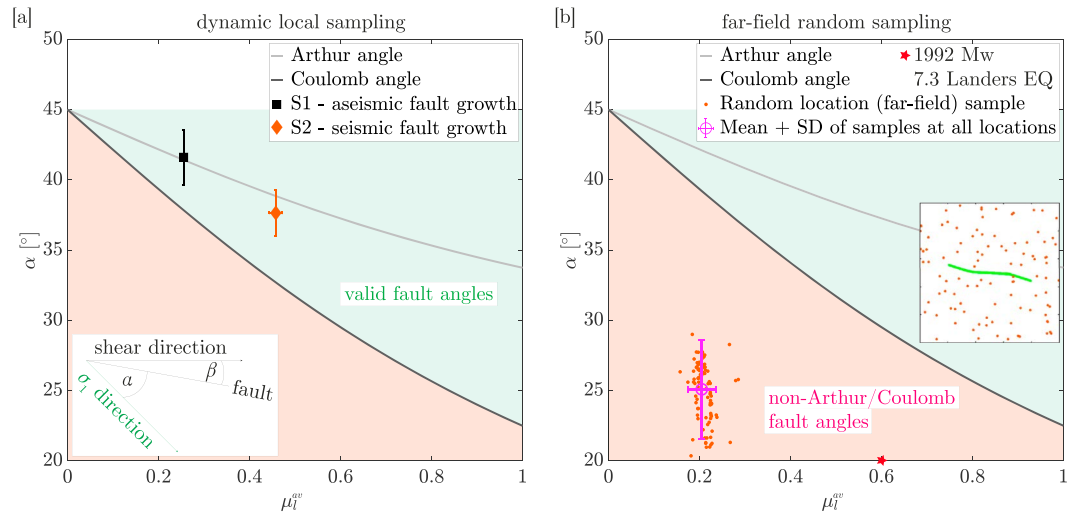
Figure 5. Relation between friction μ_l^{av} and fault angle α. μ_l^{av} is an average value obtained from the shape-independent sample box picking using three percentiles (explained at beginning of section 3 and applied in Figure 4). Angle α calculates as $\alpha_k = \sigma_{1_k}^{av} - \beta_k$, where $k = 1, 2$ indicates the respective faulting stage. β is measured relative to the E-W shearing direction, see the explanation in inset of left panel. (a) Taking dynamic local values into account. S1 and S2 plot close to the Arthur angle function and lie within the valid range of fault angles (the green-shaded polygon that is spanned between Roscoe angle (45°) and Coulomb angle). Given error bars indicate the standard deviation when using different percentiles (0.5, 0.95, 0.99) for calculating $\mu_{l_k}^{av}$ and $\sigma_{1_k}^{av}$, respectively. The angle α_k is subjected to an additional measuring error that stems from measuring β_k. This error is taken into account and was added to the vertical error bars. (b) Taking far-field random (dynamic or static) samples into account. Orange dots indicate data from 100 randomly chosen locations. Their location around the green fault is visualized within inset in (b). Data points that lie at $\alpha \approx 30°$ were sampled close to or inside the fault zone but not at the fault tip. Pink data represent mean and standard deviation taking into account data from all grid points. We only consider seismically formed fault S2 with an angle of $\beta_2 = 18.7°$. Averaged σ_1 direction in the entire model is 44.1°, thus, $\alpha = \sigma_1 - \beta_2 \sim 25.4°$. The μ_l is 0.21 on average in the entire model. Data lie within the non-Arthur/Coulomb range of fault angles (red-shaded polygon, see main text for explanation). Red star indicates the 1992 Landers earthquake (section 4.1.1). Here we assume a static friction of 0.6.

supporting information and in the repository for this publication (Preuss et al., 2019). As the rupture reaches the old fault tip of stage S1, the fault starts to bend and the fault angle β increases. The bending lasts 6 s and afterward the fault propagates seismically at an angle $\beta_2 = \pm 18.7°$ (Figures 2b, 4a, and 4c). This dynamic fault growth angle β_2 remains stable throughout the rest of the simulation. Due to the direct effect of rate- and state-dependent friction, elevated slip velocities additionally induce an increase of the friction coefficient up to $\mu_{l_2}^{av} = 0.47$ and a rotation of the average σ_1 direction to a maximum value of $\sigma_{1_2}^{av} = 65°$ (Figure 3). A clear global maximum of μ_l^{av} is observed at the fault tip and the σ_1 direction is clearly elevated in the vicinity of the fault and ahead of the fault tip (Figure 4c). In contrast, the local friction coefficient has an average value of 0.08 inside the shear band and it drops to a minimum of 0.006 within the most mature, central part of the fault. This decrease has, however, no impact on the angle of the growing faults. Due to the simultaneous jump of σ_1 direction and friction value at the fault tip, the dynamically formed fault follows the theory of the Arthur angle when applied to the elevated dynamic quantities $(\beta_2, \mu_{l_2}^{av}, \sigma_{1_2}^{av})$. Thus, the fault angle of S2 plots very close to the Arthur failure curve in Figure 5a.

In the following 27.4 s of the dynamic event the evolving fault extends by 22.3 km and the maximum slip velocity on the fault reaches 0.83 m/s before the fault hits the side boundary. We stop the simulation at the moment when the fault segment has reached a length of 36.8 km to impede boundary interaction. The rupture event shows a crack-like rupture behavior during the entire simulation, such that at every point in time the fault continues to slip (Figure 6b). At the beginning of stage S2 the amount of slip increase at the propagating fault tip is slightly lower than that in the model center, and at the end of stage S2 it is slightly higher than that in the most mature fault section. As the fault transitions to stage S2, shortly after the dynamic event has nucleated in the model center, we observe a transient increase of the rupture velocity V_r up to 1 km/s. As the rupture reaches the tip formed during stage S1 it decelerates rapidly and V_r decreases due to more energy needed to break the intact rock ahead of the fault tip (Figure 6a). In the following, V_r increases toward the end of the simulation in an unsteady, oscillatory manner. This reflects numerical
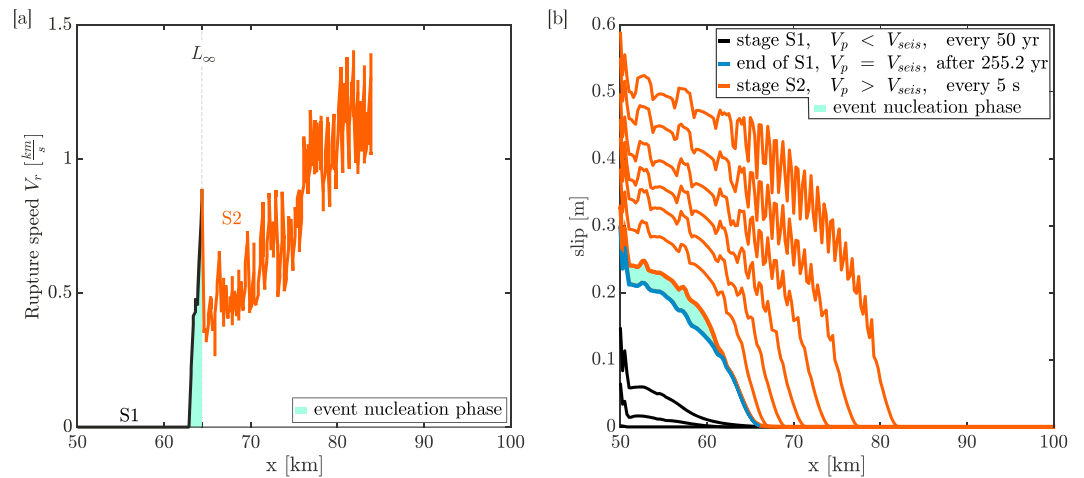
Figure 6. Rupture and slip properties during stage S2. Curve colors correspond to different stages S1 and S2 as indicated in the legend of (b). (a) Speed of the rupture front V_r along the x axis starting from the center of the model at $x = 50$ km. Event nucleation phase is indicated in turquoise, the nucleation length L_∞ is indicated by a dashed black line. (b) Slip contours, plotted at regular times, whose interval depends on V_p as indicated in the legend. End of stage S1 and the successive event nucleation phase are indicated. Stage S1 is represented by five lines, which add up to a total of 250 years. However, during the initial localization phase no slip is accumulated and thus, only three lines are visible.

noise due to the rupture cutting through the numerical grid, leading to inaccuracies in simulations and measurements. This behavior is also visible in the slip contours in Figure 6b). However, V_r never reaches the speed of around 2.5 km/s that is observed on a predefined weak fault zone in an otherwise similar model (Herrendörfer et al., 2018) because in our model energy is consumed by breaking intact rock.

3.3. Far-Field Sampling and Effects

In nature it is not possible to obtain both dynamic and local measures of an angular-frictional relation as we can do in simulations. The reason is that (i) stress and friction measurements are not feasible proximal to a propagating fault tip; (ii) dynamic measurements of these quantities during fault propagation cannot be obtained (explained in discussion section 4.1.2).

To demonstrate that wrong conclusions can be drawn from usually available far-field measurements, we imitate an off-fault borehole measurement by taking 100 samples of μ_l and σ_1 direction at random locations in our model. Next, we sample each grid point of the model domain for both quantities and individually compute mean and standard deviation of their sums, respectively.

The result, considering the seismically formed fault (S2), shows that random location measurements as well as averaged measurements from all locations plot far from Arthur angle and Coulomb angle curves (Figure 5b). They lie within a sector of the plot that can be labeled as *non-Arthur/Coulomb fault angles*, because these data points do not fulfill the classical Coulomb nor the classical Arthur failure theories. This demonstrates that if quantities to calculate the fault angle are not taken at the right location, that is, at the fault tip, and at the right time, that is, during fault formation, the apparent fault angle becomes invalid in the Coulomb/Arthur sense. The reason for this behavior is that the global average of the σ_1 direction remains at 44.1° and friction at $\mu = 0.205$. Both values are very close to their initial values. These far-field values do not change between dynamic and static phases.

3.4. Grid Size Dependence

In this section we present the effects of grid size changes on fault angles. We increase the numerical resolution by decreasing the grid size from 500 to 125 m. The reference model has the intermediate resolution of $\Delta x = 250$ m. Variations of fault angles lie within the error bars. In the low-resolution model with $\Delta x = 500$ m, the fault angle during stage S1 is $\beta_1 = 0°$ and the resolution is too low to resolve the fault inclination. The angle β is influenced by the numerical resolution (Figure 7b). Faults become steeper with increasing resolution during both faulting stages. This is because the finer the grid the better the simulation resolves the peak slip velocity of the rupture in the process zone L_b defined by Rubin and Ampuero (2005) as it approaches the fault tip formed during S1. The process zone L_b during quasi-static rupture is 2.9 km in our simulation and
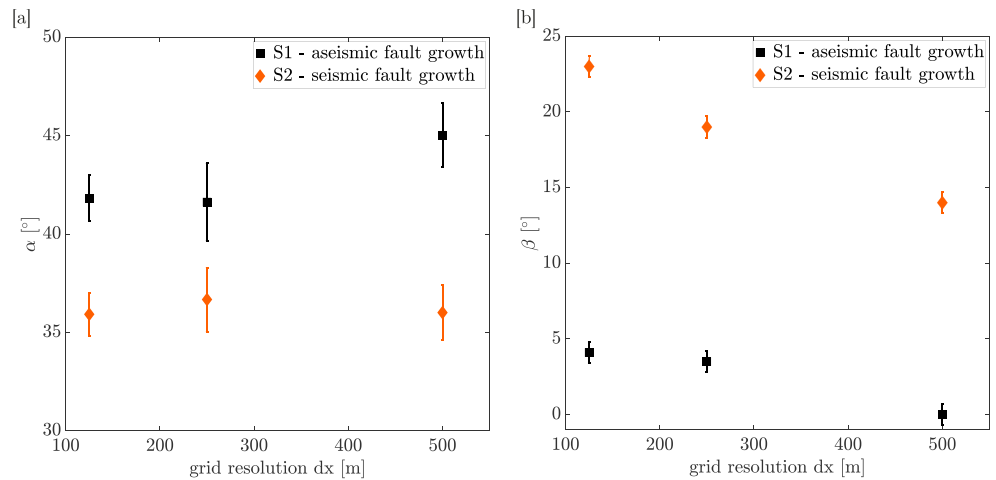
Figure 7. Relation between grid resolution and fault angles. (a) Grid resolution in meter versus angle α. Colors indicate different faulting stages. Grid size has a minor effect on the measured angles. Error bars indicate the standard deviation when using different percentiles (0.5, 0.95, 0.99) for calculating σ_1^{av} at the fault tip. The uncertainty in the measurement of β is added to this error as it is contained in the calculation of α. (b) Grid resolution in meter versus angle β. Increasing grid size results in increasing fault angles. Error bars indicate the uncertainty in the measurement of β.

is resolved with 11 grid points. During dynamic rupture propagation it decreases as shown by Herrendörfer et al. (2018). A higher V_p induces higher friction and higher stresses in the undeformed matrix at the beginning of stage S2 and hence, the fault gets steeper. In contrast, the angle α, which is used especially to assess the optimality of fault angles, is only affected marginally by resolution changes (Figure 7a). Thus, our main findings concerning the fault angles remain well-founded.

The presented numerical sensitivity analysis indicates that our results are valid for $\Delta x \leq 250$ m at which resolution we can distinguish two different stages of fault growth. Additionally, the conclusions we draw from our results, based on stress rotations and frictional increase during time-dependent fault formation are valid for aseismic and seismic fault growth.

3.5. Effect of Rate- and State-Dependent Friction Parameters and Viscosity

In this section we present the effects of changes of modeling parameters on fault angles. We systematically increase and decrease all rate- and state-dependent friction parameters by 30% to analyze the effect on fault angles. We are mainly interested in the impact of parameter changes on the angle α. Changing parameters a, b, L, μ_0, P, θ, and V_0 individually does not change the relation we observe in the reference model between angle α and maximum averaged friction value at the fault tip μ_l^{av}. All simulations plot close to the Arthur angle line. Variations lie within the measurement error described in Figure 5a and 7a. Thus, all simulations result in a Coulomb/Arthur type of faulting for both faulting stages and our main message, that fault orientation depends on whether fault growth is seismic or aseismic, holds for a range of tested parameters. The very minor degree of variation of fault angle introduced by these parameters suggests that our message holds for all parameters. This large degree of similarity results from the fact that the fault angle is mainly influenced by the friction and the stresses ahead of the fault. Essentially, the simultaneous frictional increase and the stress field rotation at the fault tip leads to the coherent result in Figure 8. Interestingly, the local time-dependent friction coefficient at the fault tip μ_l^{av} always increases by a certain amount above the assigned friction μ_0, as quantified in equation (17). This is independent of the changed parameters and thus an intrinsic feature of fault growth, especially of seismic fault growth. We aimed at keeping all numerical parameters between the individual simulations constant. The only exceptions are the cases of 30% higher a and 30% lower b, for which we had to increase the domain size to 350 km × 350 km and 1,000 km × 1,000 km, respectively. The reason is that by either increasing a or decreasing b, the nucleation size L_∞ increases dramatically, since it depends quadratically on $(b - a)$ in equation (16). This effect is strongest for a change in a, where a rather small change of 30% increases the nucleation size to 100 km. Interestingly, changing a has the highest impact on β. We discussed this in the beginning of section 4 by introducing equation (17). As a consequence, changing parameter a causes an alteration of fault angles of 1.3° and 6° for stages S1 and
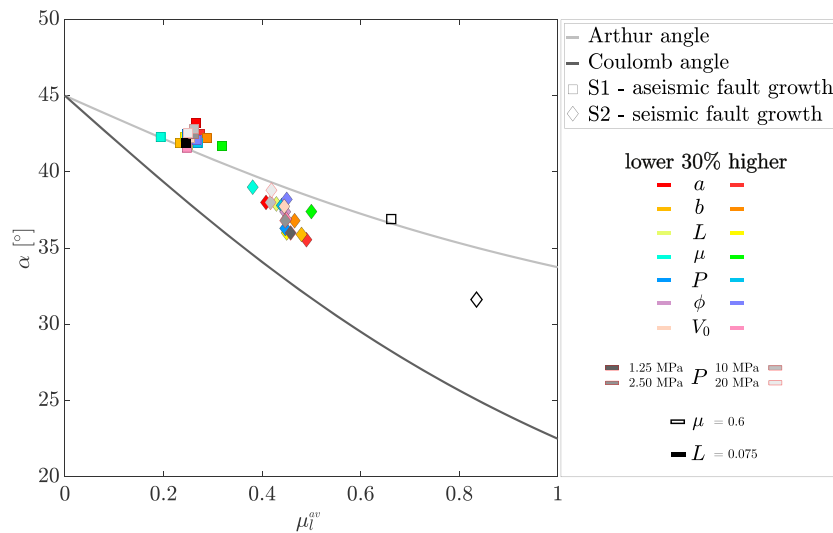
Figure 8. Relation between friction μ_l^{av} and fault angle α for a variety of rate- and state-dependent friction parameter changes. Colorful symbols represent +30% and −30% changes of all rate- and state-dependent friction parameters. Gray symbols with red contour show changes of pressure by a factor of 1/2, 1/4, 2, and 4, respectively. Void black symbols represent the case of Byerlee friction $\mu = 0.6$. Black-filled symbols represent aseismic fault growth with $L = 0.075$ m.

S2, respectively (with respect to the reference model). The change of μ_0 increases or decreases angle β in a similar manner. In contrast, changing L, P, θ, or V_0 has only minor influence on the total fault angle β.

We also modeled fault growth at different depths by increasing and decreasing pressure P by a factor of 2 and 4 ($P = 1.25$, 2.5, 10, and 20 MPa, respectively). An increase of P by a factor of 4 represents a simulation at ~2.3-km depth. As presented in equation (16), the theoretical nucleation size L_∞ is proportional to $1/P$. Indeed, an increase of P by a factor of 2 or 4 decreases the fault length at which the transition from aseismic to seismic slip occurs by factors of 2 and 4, respectively. Hence, the length of the fault generated through aseismic deformation decreases with depth. This means that fault formation occurs more readily in seismic mode at larger brittle depths. We note that a change in P has no significant impact on the angle α, as expected from equations (1)-(3). These findings suggest that our results about fault angles can be expanded to different depths of the brittle crust.

An increase of μ_0 to Byerlee friction of 0.6, which can be interpreted as the absence of pore fluid pressure (i.e., $\lambda = 0$), increases the angle β by 6° (S1) and 2.8° (S2) with respect to the reference model. However, as in all other presented models, the angle of the seismically formed fault lies in between Coulomb and Arthur fault angle (void black symbols in Figure 8).

To simulate pure aseismic fault growth we increase the value of L by a factor of 10. This increases L_∞ by an equal factor of 10. Hence, this simulation is reduced to a fault localization phase and an aseismic fault growth stage (S1), while seismic fault growth is prevented. The resulting fault angle is in agreement with the faulting stage S1 of the reference model (black-filled symbols in Figure 8). Additionally, the fault angle β_1 corresponds to the fault angle that emerges when rate- and state-dependent friction is off and the yield strength of the medium is computed with a pressure-dependent Drucker-Prager yielding criterion using a constant static friction coefficient. The angular-frictional relation between α and μ_l^{av} does not change if the initial friction coefficient of host rock and weak seed are changed independently or simultaneously in these models without rate- and state-dependent friction.

We tested various lower effective viscosities ranging from $\eta = 1 \cdot 10^{18}$ to $\eta = 1 \cdot 10^{25}$ Pa s to analyze the effect on the localization and the geometry of the forming fault. The results show that if $\eta \geq 7 \cdot 10^{19}$ Pa s, we observe the successive faulting of stages S1 and S2 with fault angles α and β agreeing with the reference model.

4. Discussion

We identified two fault growth modes that can be distinguished by both their angle β relative to the reference E-W shearing direction and by their angle α relative to the σ_1 direction. The transition between the two

modes occurs as the slip velocity reaches V_{seis} and each side of the fault (i.e., half of the entire fault) measures a length corresponding to L_∞. At this moment, a dynamic rupture event nucleates on the fault and as V_{max} keeps rising, further fault growth is driven at a greater angle. This greater angle β suggests the corresponding fault formed seismically.

Furthermore, we observe that the fault tip stress plays an important role in forming new fault surface and an alteration of the stress field surrounding the fault leads to an increase in mean stress and stress rotations there. This was similarly reported by, for example, Ando, Shaw, and Scholz (2009), Faulkner, Mitchell, Healy, and Heap (2006), and Mitchell and Faulkner (2009). We extend their view by adding that the *time-dependent value of the stresses* and the *time-dependent friction coefficient* ahead of the fault tip need to be taken into account when assessing fault angles of forming faults. These values always increase dynamically above the assigned value of μ_0 and the initial σ_1 orientation. This finding supports our first proposal. When taking into account time-dependent and local quantities of the angular-frictional relation, both aseismic and seismic fault growth mode produce faults at an Arthur angle. Formation at an Arthur angle is also observed for Riedel shear localization on a frictional interface using dynamic rupture simulations (Xu & Ben-Zion, 2013).

Our simulations show that dynamic and local friction coefficient and stress orientations increase temporally when a propagating fault tip reaches a given point (Figures 3 and 4). The location of the peak friction value $\mu_{l_2}^{av}$ at the fault tip moves and the spatial offset between $\mu_{l_2}^{av}$ and the peak slip velocity V_{max} is constant at around 2.5 km during stage S2. We conclude that the increased fault angle is slip velocity induced and is due to the slip rate dependence of the friction value in the rate- and state-dependent friction formulation. The peak friction $\mu_{l_2}^{av}$ is then given as

$$\mu_{l_2}^{av} = \mu_{pre} + a \cdot \log(\frac{V_{max}}{V_{pre}}),$$

(17)

where μ_{pre} and V_{pre} are the friction and slip velocity before the arrival of the rupture front. This estimate of $\mu_{l_2}^{av}$ arises from the acceleration of slip at a given point, which is so fast that θ does not have time to evolve. The stress increase ahead of the rupture is due to dynamic stress transfer from the slipping region.

In addition, we present a way to assess whether a natural fault formed seismically or aseismically by mimicking far-field measurements in our model:

1. A fault formed *aseismically* when far-field friction and the angle α between fault and far-field σ_1 direction suggest a *valid, Coulomb/Arthur fault*.
2. A fault formed *seismically* when far-field friction and the angle α between fault and far-field σ_1 direction suggest a *nonvalid, non-Arthur/Coulomb fault*.

This distinction is possible, because an aseismically formed fault always results in a valid Arthur fault angle, independent on location and time of the measurement. In contrast, a seismically formed fault can only correctly be assessed as Coulomb/Arthur fault when considering local dynamic (time-dependent) friction and stress orientation at the fault tip. We note that these implications are only true if the far-field stresses are constant on the timescale considered for fault assessment. Long-term, large-scale tectonic rearrangements can alter stress orientations. However, since most stress measurements are obtained near term, this issue becomes minor.

We pursue this line of reasoning in the following section by considering the 1992 Landers earthquake.

4.1. Comparison to Natural Examples
4.1.1. The 1992 Landers Earthquake
We consider here the example of the 1992 M_w 7.3 Landers earthquake, which occurred off the main San Andreas fault to which it lies at a high angle (~47°). Precisely, it nucleated on the Johnson Valley fault and then ruptured the Kickapoo, Homestead Valley, Emerson and the Camp Rock faults (Plesch et al., 2007; Rockwell et al., 2000; Sieh et al., 1993). Of these faults the only unknown fault at the time was the Kickapoo fault (Sieh et al., 1993). Thus, the Kickapoo fault segment might have linked the previously known faults. The other fault segments were believed to have been in the process of formation just recently before the Landers event (Nur et al., 1989; Ron et al., 1981). Especially insightful were at least four previous earthquakes in that region that had similar rupture directions in the four decades before the 1992 Landers rupture (Nur et al., 1993). The hypothesis of a new Landers-Mojave fault line was based on observations and the fact that the well-developed N-W oriented strike-slip faults in the region (gray lines in Figure 9) and the main San
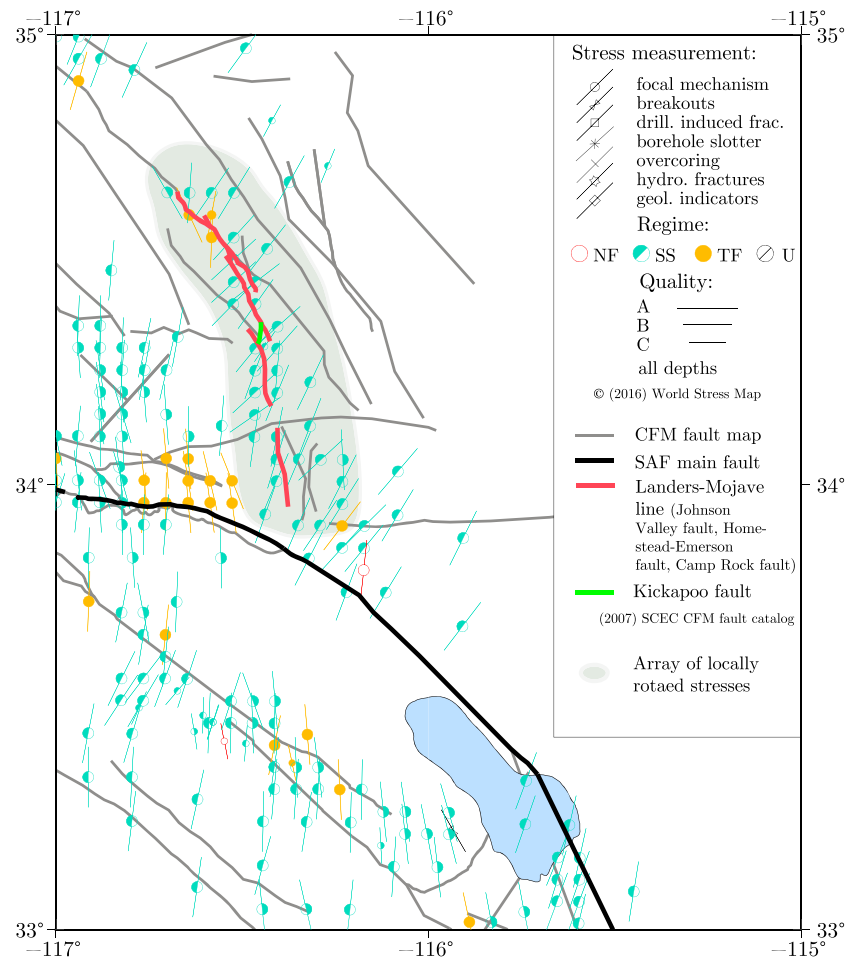
Figure 9. Stress map of the eastern California shear zone from World Stress Map Project (Heidbach et al., 2018) combined with Community Fault Model (CFM) fault catalog from Southern California Earthquake Center (Plesch et al., 2017; Plesch et al., 2007). Colored symbols in turquoise, orange, and red represent σ_1 orientations obtained from focal mechanisms. SS = strike slip; TF = thrust faulting; NF = normal faulting. Red lines represent Landers-Mojave fault line (Johnson Valley fault, Homestead Valley fault, Camp Rock-Emerson fault). Black line marks San Andreas main fault. Gray lines are the before 1992 mapped faults. Green line is the Kickapoo fault. Gray-green shaded area marks locally rotated stresses.

Andreas fault (black line in Figure 9) are mechanically unfavorably oriented with respect to the maximum tectonic compressional stresses σ_1 (Nur et al., 1993; Stein et al., 1992; Zoback et al., 1987, 1991). As a matter of fact, the N-W oriented strike-slip faults and the main San Andreas fault are oriented at a high angle (~90°) to the regional σ_1 orientation. The hypothesis of a new forming fault line follows because new faults form when the primary fault becomes critically misaligned with the principal stresses or inefficient (Fattaruso et al., 2016; Scholz et al., 2010; Sibson et al., 2011). We here assume that fault linkage, like in the case of the Kickapoo fault, can potentially follow either of the two growth modes, too. To prove our assumption we want to analyze the stress field in the Eastern California Shear Zone in the same manner as done in section 3.3 and discussed at the beginning of section 4, because this has the potential to give insights about the mode of fault growth of the Kickapoo fault (aseismic vs. seismic). However, we emphasize here that this analysis is not necessarily based on the assumption that the Kickapoo fault formed as a result of the Landers earthquake but rather that it formed at any point in time.

The Kickapoo fault is approximately oriented at 10° with respect to N-S. Thus, it is parallel to the remote stress field (σ_1 direction of 10°) of the region (Figure 9). According to all classical faulting theories, it is not prone to have formed in this stress field. The local stresses around the Landers-Mojave fault line including the Kickapoo fault have an orientation of ~30° (green-gray polygon in Figure 9). Hence, the angle α between the local σ_1 direction and the Kickapoo fault is low and approximately at 20°. Assuming Byerlee friction of

0.6 the angular-frictional relation for this fault would plot in the non-Arthur/Coulomb fault angle range in Figure 5b. Thus, consideration of the local stress field brings the fault closer to the prediction of the Arthur or Coulomb faulting theories. However, it is still far from both. Now, we want to assume that the local stresses had rotated during the propagation of a dynamic rupture as predicted by our study, that is, they might have rotated by an angle of 20° (same angle as between simulation stages S1 and S2). This would result in a dynamic local σ_1 direction of ~50°. If, furthermore, it is right that fault growth is controlled by these local time-dependent quantities, as suggested by our study, the Kickapoo fault would have formed according to the Arthur faulting criterion. This brings the fault in the valid range of fault angles in Figure 5b.

Our conclusion is that the Kickapoo fault might but must not have formed due to the 1992 Landers earthquake. Based on our simulation results we believe that the fault has formed seismically, which seems to be confirmed by other studies (see above). Additionally, we propose that a fault at an angle of ≳25° to the parent fault has formed seismically. This follows from the combined analysis above and is likely only true if fault growth was not affected by surrounding structural heterogeneities.

We gain another insight from our brief analysis: Fault formation changes the stress field adjacent to the formed fault and that far-field stresses are potentially not affected by the formation of the new fault network as they had a similar orientation before the 1992 event. Our simulation results have implied this proposal. The proposal would be true even if the fault was a blind fault and formed not due to the 1992 seismic event, but before.

4.1.2. Sampling Friction Angles and Stress Orientations

Stress measurements like well bore breakouts, drilling-induced fractures, and in situ stress measurements (overcoring, hydraulic fracturing, and borehole slotter) do not exist in immediate proximity (<1 km) to the fault and earthquake focal mechanisms, on the other hand, are not suitable to determine friction coefficients (pers. communication: Heidbach et al., 2018). An exception to the lack of in situ stress measurements is the SAFOD drilling into the San Andreas fault at Parkfield (Hickman & Zoback, 2004; Zoback et al., 2010). However, even in this location it is not possible to measure μ and σ_1 direction during the dynamic rupture propagation. Especially, it is not possible to sample data during fault growth as the sampling location would have to move with the propagating fault tip. Furthermore, SAFOD is clearly not located at the current fault tip of a San Andreas fault segment. The stress and friction data we obtain in nature are static ones compared to the timescale of an earthquake and they are subject to a large error. Furthermore, they can be interpreted as reflecting a far-field behavior of the stress field, although they are obtained at a definite location. In this paper we show how these static far-field values can be used to assess whether a fault formed seismically or aseismically.

4.1.3. Implication for Fault Maturation in a Homogeneous Weak Material

Our modeling indicates that a single sequence of aseismic and seismic fault growth can occur on faults that are free to grow in isolation in a homogeneous stress field, that is, without being surrounded by other faults. Additional faults would add structural complexity that would result in stress heterogeneities. Furthermore, the material is weak (low initial friction and low initial state contrast). These two factors facilitate fault growth in contrast to the case of material with a higher strength or existing stress heterogeneities. Thus, a single seismic event can form a several-tens-of-kilometer-long fault because of dynamically elevated stresses at the fault tip. These result in a high potential strain energy in the vicinity of the evolving fault and feed fault growth. We expect that strong prevailing heterogeneity in structure or stresses might challenge the behavior described above. On a relatively short 100-year timescale, we expect that the propagation of faults may mostly operate by linking of existing structures, as in the Landers example. The linking segments must not necessarily be small. Further, they can operate either seismically or aseismically, depending on various factors as, for example, the theoretical nucleation size of an event, the strength of the host rock, the regional stress field variability, and the curvature of the preexisting structure. On the long-term, we expect faults also propagate by continuous lateral extension at fault tips, as shown in the example of the North Anatolian Fault (Şengör et al., 2004). In a future work we will study more complex faulting behavior including the evolution of fault networks by alternating sequences of aseismic and seismic fault growth, fault linkage and branching and the effect of stress field heterogeneities.

4.1.4. Relation to Fault Bends, First-Order Splay Faults and Normal or Thrust Faults

Many faults in nature have kinks or bends (e.g., Biasi & Wesnousky, 2017, and references therein). Our results provide a possible explanation for fault bends. When a fault transitions from aseismic to seismic fault growth as slip velocities increase, the fault line will bend, change its direction, and the absolute fault angle

β will increase. The so generated seismic fault in our simulation forms under a typical splay fault angle and fulfills all criteria to be defined as classical first-order splay fault (Scholz et al., 2010). Splay faulting at an average angle of $\pm17°$ from the San Andreas fault deviates only slightly from the bend angle of $\pm15.2°$ we observe between stages S1 and S2 (Ando et al., 2009). This might imply that branching as well as bending starts once a rupture nucleated on the main fault and once it reached a high enough slip velocity. In the case of our simulation the main fault is the aseismic fault formed during S1. As this high slip velocity is reached the stress field rotates close to the rupture tip and the friction value increases locally according to equation (17). Consequently, the primary fault becomes misaligned with the rotated stresses, which is a condition for splay fault formation (Scholz et al., 2010). If then the off-fault material is prone to undergo yielding a new branch/bend will start under a different and more optimal oriented angle than the main fault. In essence, we assume that splay faulting and fault bending are related processes if the latter originated from elevated slip velocities during seismic fault growth. The difference between both cases is that a fault bend constitutes the continuation of the main fault while a splay fault branch is a secondary structure. The difference is a geometrical one: The onset of bending/branching depends on whether the transition to high enough slip velocities is reached at the main fault tip or before, respectively. Thus, it is debatable if the fault in S2 can be considered as a classical splay fault. However, we argue that both types might form in response to the same processes when neglecting structural heterogeneities.

As shown by Poliakov et al. (2002), in mode II, dynamic stresses near a rupture tip are maximal on the extensional side at one certain angle, when rupture speed is sufficiently fast. This implies rupture branching or bending at that angle. The same study shows that for mode III the dynamic stresses at a rupture tip have two symmetric maxima, which may predict forking rather than bending. Based on these findings we assume that fault growth in normal or thrust faults is different than in mode II strike slip and likely results in forking. However, in both cases fault geometry changes at fast (seismic) rupture speeds. Additionally, many parameters change with depth, which is of great importance in vertical mode III fault growth and ignored in our current model.

4.1.5. Relation to Slip Spectrum

The second proposal of this paper is that different modes of fault growth may exist, similarly to the existence of different modes of fault slip. Natural faults generate a wide slip spectrum ranging from dynamic, coseismic slip to fault creep (e.g., parts of the Haiyuan Fault in China; Jolivet et al., 2013). Additionally, decades of observations demonstrate that small, moderate, and large earthquakes occur on creeping shallow crustal faults around the world (Harris, 2017; Lindsey et al., 2014). Evidence that seismic and aseismic slip coincide on the same fault segment is rare; however, few observations exist: Four seismically inactive patches have different locations after the Izmit (before the Düzce) and after the Düzce mainshock (Bohnhoff et al., 2016), which can be interpreted as shifting of aseismic fault patches along the fault. Furthermore, two of these inactive fault patches are colocated or coincide with the maxima of the coseismic slip (Bohnhoff et al., 2016). Areas of coseismic slip coincide with fault areas that are otherwise aseismic on the Calaveras fault, as shown for the 1979 Coyote Lake and the 1984 Morgan Hill earthquake (Oppenheimer et al., 1990). Additionally, an 8-month slow-slip event triggered progressive nucleation of the 2014 Chile megathrust, that broke both frictional asperities and surrounding conditionally stable areas, which, before, hosted slow-slip and superimposed seismic signals (Socquet et al., 2017). The above observations are supported by recent modeling studies in which slip can change from slow-slip to fast rupture events on the same fault segment (Noda & Lapusta, 2013; Veedu & Barbot, 2016). Thus, faults generate a wide slip spectrum. In this study we additional show that fault growth is equally accompanied by varying slip velocities. We furthermore show that, as a result of these varying slip velocities, two fault growth modes exist.

4.2. Seismic Wave Analysis

We record generated seismic waves at two stations whose location is displayed in Figure 2b. The seismogram in Figure 10a plots the time series of time derivatives of v_x and v_y velocities. The accelerometer at location 1 records the E-W component first, while the N-S ground acceleration is first recorded at location 2. Taking into account that the start of recording of the seismogram is right at the beginning of stage S2, the approximate onset of all arrivals between 5 and 10 s agrees well with the theoretical P wave speed c_s of 5.6 km/s (using a P wave/S wave ratio c_s/c_s of 1.7) and the averaged distance of the two locations from the event nucleation point of ~40 km, yielding ~7.1 s travel time. The dominant frequency content of the waveforms is below 2 Hz (Figure 10b). This value is higher than that in the case of a rupture event on a predefined fault in a similar model, in which the dominant frequency content is below 0.5 Hz (Figure 9 in Herrendör-
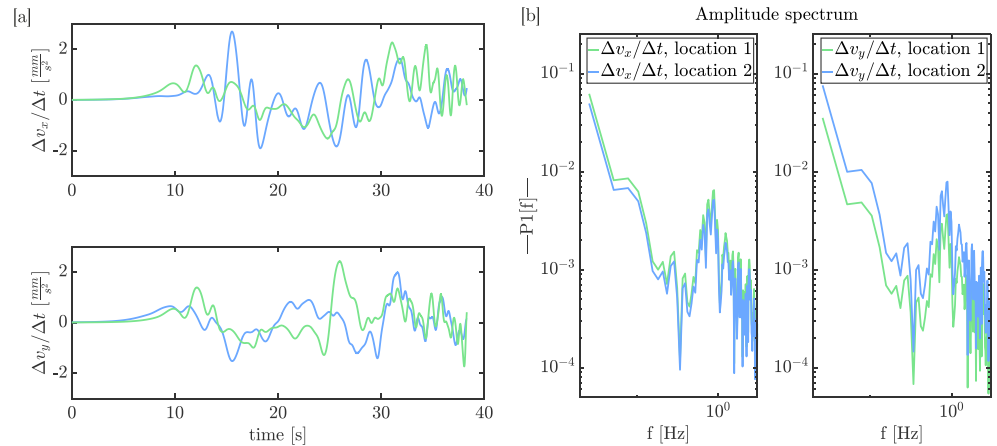
Figure 10. Seismic wave properties during stage S2. (a) Time series of time derivatives of E-W v_x (upper panel) and N-S v_y (lower panel) velocities at two locations as indicated with the correspondingly colored crosses in Figure 2b. The two accelerometers are located at equivalent positions as in Herrendörfer et al. (2018). (b) Amplitude spectra of the waveforms in (a).

fer et al. (2018)). Dynamic earthquake rupture on a newly forming fault produces a higher-frequency signal because the strength drop is larger for a fault that is in the process of being created. The initially intact rock is penetrated by the approaching fault tip and thus dynamically weakened. During this weakening phase the fault is still stronger than the predefined fault that is continuously weak. This means that the material at the locations through which the fault propagates evolves from a relatively strong material (higher μ_l) to a weaker material (lower μ_l). A higher $(\mu_l^s - \mu_l^d)$ implies a stronger high-frequency content of the source, because the highest-frequency cutoff of the source is positively dependent on the material strength:

$$f_{\max} = \frac{V_r}{\Lambda} \sim \frac{V_r}{\frac{GL}{(\sigma(\mu_l^s - \mu_l^d))}},$$

(18)

where Λ is the dynamic cohesive zone length (Herrendörfer et al., 2018; Lapusta & Liu, 2009), μ_l^s and μ_l^d are static and dynamic local friction coefficients, respectively.

4.3. Modeling Limitations and Uncertainties

In nature, fault growth is a three-dimensional process. With our presented 2-D plane strain model we neglect the third dimension and instead assume perfectly vertical fault surfaces. This is valid in a first-order sense; however, various natural strike-slip faults can have changing dip angles with depth (e.g., Ross et al., 2017). Another drawback of our 2-D simulations is the finiteness of the seismogenic depth. A finite seismic layer limits the stress concentration at the fault tip, which in turn limits the spatial extent of plasticity outside the main fault (Ampuero & Mao, 2017) and the energy available for a dynamic rupture to keep growing (Weng & Yang, 2017). Potentially, in 3-D the dynamic rupture would stop spontaneously after some propagation distance larger than the seismogenic depth. A repetition of this cycle might then lead to a complex intermittent sequence of aseismic and seismic fault growth, which can be supported by stronger host rock, misaligned faults, and stress rotations. At much longer timescales, viscous relaxation below the crust could counteract this effect of seismogenic depth (Ampuero & Mao, 2017).

Our simulations and theoretical predictions suggest that the fault length that forms through aseismic deformation decreases with an increase in depth (section 3.5). However, these simulations exclude a temperature-dependent rheology that would imply rheology changes with depth and they ignore a stress concentration at the base of the seismogenic zone. Temperature has a first-order effect on the rate- and-state-dependent friction parameters a and b, which in turn are expected to affect the length of stage S1 as encapsulated in equation (16). Stress concentrations at the base of the seismogenic zone are induced by deeper fault creep. This allows earthquakes to start at depth while the rest of the fault at shallower depth still has low stress, giving a low depth-average apparent fault strength. We thus note that the depth dependence of L_∞ implied by our 2-D model might be oversimplified and 3-D simulations that take depth-dependent

variations into account are hence needed to study to which degree active fault geometry is controlled by conditions at depth.

Additionally, changes of frictional parameters and material parameters (e.g., shear modulus) with plastic strain are not taken into account in our simulations. We note that our modeling assumes elastic isotropy and no dilation. However, observations of natural faults display anisotropy in their damage zones, and evidence for volume changes during their activity (Brace et al., 1966; Hamiel et al., 2009; Li et al., 2015; Misra et al., 2015; Nasseri et al., 2010; Peacock & Sanderson, 1992; Rawling et al., 2002; Tarasewicz et al., 2005; Woodcock et al., 2007). In this respect our model is a simplification as we ignore anisotropy, poroelasticity, or dilatant volume changes. We expect that these ingredients could potentially affect slip behavior but not the main message of this study because it will still be the local time-dependent values of friction and σ_1 direction that control the fault angle. Furthermore, we acknowledge that we use a rate-weakening bulk material. Steady state rate weakening has been documented for a wide range of sliding conditions in rocks (e.g., Dieterich, 1979, 1978; Di Toro et al., 2011; Ruina, 1983), but bulk rheology might be rate strengthening. The grid size dependence of the angle β (section 3.4) is a limitation of our model that we will address in a future study. We aim at proposing and testing one alternative invariant continuum-based rate- and state-dependent friction formulation for fault width W, such that during the strain localization phase W adapts dynamically as a function of evolving material parameters (e.g., Manning et al., 2007). There is a need to introduce a length scale in the viscoelastoplastic formulation making it nonlocal (Eringen, 1983). A phenomenological plasticity law (Fleck et al., 1994) or a continuum theory where strain rate is uniform within a shear band of finite thickness in a gouge layer of nominal thickness and zero outside this zone (Sleep et al., 2000) have been demonstrated to be heuristic fixes. Furthermore, we note here that modeling arbitrary crack growth is an active area of research in the computational mechanics community (e.g., Borden et al., 2012; Liu & Borja, 2008).

4.4. Rate- and State-Dependent Friction in a Continuum

The classical Dieterich-Ruina rate-and-state friction framework has been validated for sliding on predefined rock surfaces. In classical seismic cycle simulations, discontinuous brittle deformation occurs in form of slip on an infinitely thin, predefined fault. It is the magnitude of slip velocity that enters into the rate-and-state formalism. In contrast, in our continuum mechanics approach, plastic deformation is treated as strain, represented in the form of a shear band of finite width and can occur everywhere (see section 2.1). The difference in the concepts of slip and strain requires that the slip rate magnitude in the classical rate-and-state friction framework is related to the second plastic strain rate invariant in the continuum mechanics description (Herrendörfer, 2018). This is achieved by scaling the magnitude of the slip rate to the second invariant of plastic strain rate (see equation (13)). Further research including the comparison to analog models is needed to test and further refine the continuum-based constitutive relationship describing self-consistently both localization toward a fault and deformation within the fault (Herrendörfer, 2018).

4.5. Role of Cohesion

In our simulations we assume the material has zero residual strength ($C = 0$ MPa), as typically assumed in rate- and state-dependent friction modeling. This is justified by numerical tests from Herrendörfer, 2018 (2018, section 7.2.2), which showed that a cohesionless fault embedded produces the same results in a host rock with or without cohesion. Additionally, Herrendörfer, 2018 (2018, section 7.2.2) demonstrated that cohesion applied along the fault does not change the overall earthquake cycle behavior apart from more time is required to generate the first earthquake. Herrendörfer, 2018 (2018, section 7.2.2) follows from these tests that adding cohesion has essentially the same effect as increasing the reference effective static friction μ_0 by an equivalent amount (Herrendörfer, 2018, section 7.2.2). To confirm that cohesion has no influence on fault angles during rapid fault growth we present a simulation with a cohesive host rock in section 3.5. We note that a nonzero cohesion in the host rock does not change fault angles and thus, will not change our conclusions. Furthermore, the higher initial state in the host rock compared to the weak inclusion can be considered to be equivalent to a higher cohesion there.

Interestingly, the local time-dependent friction coefficient at the fault tip μ_l^{av} always increases a certain amount above the assigned friction μ_0. This is independent of the changed parameters and thus an intrinsic feature of fault growth, especially of seismic fault growth.

These values always increase dynamically above the assigned value of μ_0 and the initial σ_1 orientation.

5. Conclusions

We systematically studied the process of spontaneous fault growth using a model that allows for the spontaneous evolution of a fault governed by an invariant rate- and state-dependent friction formulation. With this model we investigated how fault angles evolve during different stages of fault formation and propagation. Our two hypotheses are as follows: (1) Fault angles are defined by evolving local instantaneous near-tip stress field and friction coefficient during all phases of fault formation. (2) Similarly to the existence of slow and fast modes of fault slip, seismic and aseismic modes of fault growth may exist. Our findings confirm these hypotheses and comprise the following:

1. Two end member fault growth modes are distinguished in a generic model of a strike-slip fault zone, which are *aseismic* and *seismic* fault growth. After an early stage of shear band localization faults grow aseismically until they reach the nucleation size of a dynamic event. As the event nucleates, the slip velocity increases and the growing fault transitions to a seismic propagation mode. The result is a greater strike angle of the growing fault, which leads to a fault bend. This finding supports our second hypothesis.

2. The increase of the total fault angle at the transition between the aseismic and seismic faulting stage is induced by slip rate. It is due to the slip rate dependence of the friction value in the rate- and state-dependent friction formulation. Seismic fault growth causes significantly elevated dynamic stresses, stress orientations, and friction coefficient at and ahead of the propagating fault tip. These local dynamic quantities increase significantly above the assigned reference static friction coefficient μ_0 and the initial σ_1 orientation. This behavior causes the increase in fault angle and holds for a range of tested parameter changes. These findings support both our hypotheses.

3. With respect to the remote stress field, aseismic fault growth agrees with Coulomb/Arthur failure criteria, while the seismic fault growth stage does not agree with it. However, in relation to local and dynamic quantities, both fault growth modes obey the Coulomb/Arthur failure theory. It follows that all faults form as predicted by the failure criterion of Mohr-Coulomb because they grow according to the state of stress prevailing at the time of genesis. Consequently, the assessment of the optimality of fault angles requires the consideration of local near-tip stress field and friction coefficient in a dynamic sense, that is, during the phase of fault formation. This finding further supports our first hypothesis.

4. We show that the main conclusions are not affected by numerical and physical parameters.

5. The four previous points suggest that seismically formed faults can be distinguished from aseismically formed faults in two ways in nature:

    a. By comparing them to far-field stress orientations: An aseismically formed fault will be predicted as a Coulomb/Arthur fault, while a seismically formed fault will be predicted as a non-Arthur/Coulomb fault. The reason is that local stress field and friction value are marginally altered during aseismic fault growth, but they are significantly altered during the seismic stage of propagation. However, the far-field stress field and far-field samples of the friction value are not affected by local fault growth. This conclusion underlies the assumption that the far-field stresses are constant on the timescale considered for fault assessment. That is mostly valid as stress measurements are obtained near term. The above statement is supported by the analysis of the stress field in the region of the 1992 Landers earthquake where only the near-fault stresses have rotated.

    b. By comparing them to the shearing direction: In relation to the shearing direction seismically formed faults have a greater angle than aseismically formed faults. We propose that a fault at an angle $\gtrsim 25°$ to the parent fault has formed in seismic mode. We obtain this value from the analysis of the stress field in the Eastern California Shear Zone where the Kickapoo fault potentially formed seismically near term to the 1992 Landers earthquake. We make this statement under the assumption that fault growth was not effected by surrounding structural heterogeneities.

6. The fault orientation could be used to predict the dynamic stress field during seismic fault formation, which is otherwise not measurable.

7. Our results have implications for big strike-slip systems as, for example, the San Andreas fault. The stress field surrounding mature fault zones is often misaligned with existing faults. This is due to a combination of the following factors: reorientation of the stress field during fault formation, long-term reorientation of stresses due to strain accumulation, structural complexity, for example, induced by nearby faults, and general heterogeneity of stresses on a local to far-field scale. The misalignment of the stress field with existing faults facilitates the reactivation of inactive and potentially blind or unknown fault branches and

can additionally cause formation of new faults. Our approach gives an indication how such new faults can grow and at which angle.

Appendix A: Online Repository

A video showing the temporal evolution of the fault and also the generation of shear and pressure waves is in the repository of this paper (Preuss et al., 2019) and can be found under this link.

References

Ampuero, J. P., & Mao, X. (2017). Upper limit on damage zone thickness controlled by seismogenic depth. *Fault Zone Dynamic Processes: Evolution of Fault Properties During Seismic Rupture*, *227*, 243. https://doi.org/10.1002/9781119156895.ch13

Anderson, E. M. (1905). The dynamics of faulting. *Transactions of the Edinburgh Geological Society*, *V8*(February 2010), 387–402. https://doi.org/10.1080/10942911003754718

Anderson, E. M. (1942). The dynamics of faulting. *Transactions of the Edinburgh Geological Society*, *8*, 387–402.

Ando, R., Shaw, B. E., & Scholz, C. H. (2009). Quantifying natural fault geometry: Statistical of splay fault angles. *Bulletin of the Seismological Society of America*, *99*(1), 389–395. https://doi.org/10.1785/0120080942

Andrews, D. J. (1976). Rupture propagation with finite stress in antiplane strain. *Journal of Geophysical Research*, *81*(20), 3575–3582. Retrieved from https://doi.org/10.1029/JB081i020p03575

Andrews, D. J. (2005). Rupture dynamics with energy loss outside the slip zone. *Journal of Geophysical Research*, *110*, B01307. https://doi.org/10.1029/2004JB003191

Arthur, J. R. F., Dunstan, T., Al-Ani, Q., & Assadi, A. (1977). Plastic deformation and failure in granular media. *Géotechnique*, *27*(1), 53–74.

Aydin, A., & Berryman, J. G. (2010). Analysis of the growth of strike-slip faults using effective medium theory. *Journal of Structural Geology*, *32*(11), 1629–1642. Retrieved from https://doi.org/10.1016/j.jsg.2009.11.007

Biasi, G. P., & Wesnousky, S. G. (2017). Bends and ends of surface ruptures. *Bulletin of the Seismological Society of America*, *107*(6), 2543–2560. Retrieved from https://doi.org/10.1785/0120160292

Bohnhoff, M., Ickrath, M., & Dresen, G. (2016). Seismicity distribution in conjunction with spatiotemporal variations of coseismic slip and postseismic creep along the combined 1999 Izmit-Düzce rupture. *Tectonophysics*, *686*, 132–145. Retrieved from https://doi.org/10.1016/j.tecto.2016.07.029

Borden, M. J., Verhoosel, C. V., Scott, M. A., Hughes, T. J., & Landis, C. M. (2012). A phase-field description of dynamic brittle fracture. *Computer Methods in Applied Mechanics and Engineering*, *217-220*, 77–95. Retrieved from https://doi.org/10.1016/j.cma.2012.01.008

Brace, W. F., Paulding, B. W., & Scholz, C. (1966). Dilatancy in the fracture of crystalline rocks. *Journal of Geophysical Research*, *71*(16), 3939–3953. https://doi.org/10.1029/jz071i016p03939

Brantut, N., Heap, M. J., Baud, P., & Meredith, P. G. (2014). Rate- and strain-dependent brittle deformation of rocks. *Journal of Geophysical Research: Solid Earth*, *119*, 1818–1836. Retrieved from https://doi.org/10.1002/2013JB010448

Buiter, S. J. H. (2012). A review of brittle compressional wedge models. *Tectonophysics*, *530-531*(0040), 1–17. Retrieved from https://doi.org/10.1016/j.tecto.2011.12.018

Buiter, S. J. H., Schreurs, G., Albertz, M., Gerya, T. V., Kaus, B., Landry, W., et al. (2016). Benchmarking numerical models of brittle thrust wedges. *Journal of Structural Geology*, *92*, 140–177. https://doi.org/10.1016/j.jsg.2016.03.003

Bürgmann, R., Pollard, D. D., & Martel, S. J. (1994). Slip distributions on faults: Effects of stress gradients, inelastic deformation, heterogeneous host-rock stiffness, and fault interaction. *Journal of Structural Geology*, *16*(12), 1675–1690. https://doi.org/10.1016/0191-8141(94)90134-1

Byerlee, J. (1978). Friction of rocks. *Pure and Applied Geophysics PAGEOPH*, *116*(4-5), 615–626. https://doi.org/10.1007/BF00876528

Choi, E., & Petersen, K. D. (2015). Making Coulomb angle-oriented shear bands in numerical tectonic models. *Tectonophysics*, *657*, 94–101. Retrieved from https://doi.org/10.1016/j.tecto.2015.06.026

Cooke, M. (1997). Fracture localization along faults with spatially varying friction. *Journal of Geophysical Research*, *102*, 22,425–22,434.

Cowie, P. A., & Scholz, C. H. (1992a). Growth of faults by accumulation of seismic slip. *Journal of Geophysical Research*, *97*(B7), 11,085–11,095. Retrieved from https://doi.org/10.1029/92JB00586

Cowie, P. A., & Scholz, C. H. (1992b). Physical explanation for the displacement-length relationship of faults using a post-yield fracture mechanics model. *Journal of Structural Geology*, *14*(10), 1133–1148. https://doi.org/10.1016/0191-8141(92)90065-5

Di Toro, G., Han, R., Hirose, T., De Paola, N., Nielsen, S., Mizoguchi, K., et al. (2011). Fault lubrication during earthquakes. *Nature*, *471*(7339), 494–499. https://doi.org/10.1038/nature09838

Dieterich, J. H. (1978). Time-dependent friction and the mechanics of stickslip. *Pure and Applied Geophysics PAGEOPH*, *116*(4-5), 790–806. https://doi.org/10.1007/BF00876539

Dieterich, J. H. (1979). Modeling of rock friction: 1. Experimental results and constituve equations. *Journal of geophysical research*, *84*(9), 2161–2168. Retrieved from https://doi.org/10.1007/BF00876539

Dieterich, J. H. (1981). Constitutive properties of faults with simulated gouge. *Geophysical Monograph Series*, *24*, 103–120. Retrieved from https://doi.org/10.1029/GM024p0103

Drucker, D. C., & Prager, W. (1952). Soil mechanics and plastic analysis or limit design. *Quarterly of Applied Mathematics*, *10*(2), 157–165. Retrieved from https://doi.org/10.1090/qam/48291

Du, Y., & Aydin, A. (1995). Shear fracture patterns and connectivity at geometric complexities along strike-slip faults. *Journal of Geophysical Research*, *100*(95), 93–102.

Erdogan, F. (1968). Crack propagation theories, (2nd ed.). In H. Liebowitz (Ed.), *Fracture: An advanced trea- tise, math. fundam* (pp. 497–590). Academic, San Diego, Calif: NASA; United States.

Eringen, A. C. (1983). Theories of nonlocal plasticity. *International Journal of Engineering Science*, *21*(7), 741–751. https://doi.org/10.1016/0020-7225(83)90058-7

Fang, Z., & Dunham, E. M. (2013). Additional shear resistance from fault roughness and stress levels on geometrically complex faults. *Journal of Geophysical Research: Solid Earth*, *118*, 3642–3654. https://doi.org/10.1002/jgrb.50262

Fattaruso, L. A., Cooke, M. L., Dorsey, R. J., & Housen, B. A. (2016). Response of deformation patterns to reorganization of the southern San Andreas fault system since ca. 1.5 Ma. *Tectonophysics*, *693*, 474–488. Retrieved from https://doi.org/10.1016/j.tecto.2016.05.035

Faulkner, D. R., Mitchell, T. M., Healy, D., & Heap, M. J. (2006). Slip on 'weak' faults by the rotation of regional stress in the fracture damage zone. *Nature*, *444*(7121), 922–925. https://doi.org/10.1038/nature05353

Fleck, N. A., Muller, G. M., Ashby, M. F., & Hutchinson, J. W. (1994). Strain gradient plasticity: Theory and experiment. *Acta Metallurgica Et Materialia*, *42*(2), 475–487. https://doi.org/10.1016/0956-7151(94)90502-9

Fletcher, J. M., Oskin, M. E., & Teran, O. J. (2016). The role of a keystone fault in triggering the complex El Mayor-Cucapah earthquake rupture. *Nature Geoscience*, *9*(4), 303–307. https://doi.org/10.1038/ngeo2660

Fossum, A. F., & Freund, L. B. (1975). Nonuniformly moving shear crack model of a shallow focus earthquake mechanism. *Journal of Geophysical Research*, *80*(23), 3343–3347. Retrieved from https://doi.org/10.1029/JB080i023p03343

Freund, L. B. (1972a). Crack propagation in an elastic solid subjected to general loading? I. Constant rate of extension. *Journal of the Mechanics and Physics of Solids*, *20*(3), 129–140. Retrieved from https://doi.org/10.1016/0022-5096(72)90006-3

Freund, L. B. (1972b). Crack propagation in an elastic solid subjected to general loading? II. Non-uniform rate of extension. *Journal of the Mechanics and Physics of Solids*, *20*(3), 141–152. Retrieved from https://doi.org/10.1016/0022-5096(72)90007-5

Gerya, T., & Yuen, D. A. (2003). Characteristics-based marker-in-cell method with conservative finite-differences schemes for modeling geological flows with strongly variable transport properties. *Physics of the Earth and Planetary Interiors*, *140*(4), 293–318. https://doi.org/10.1016/j.pepi.2003.09.006

Gerya, T., & Yuen, D. A. (2007). Robust characteristics method for modelling multiphase visco-elasto-plastic thermo-mechanical problems. *Physics of the Earth and Planetary Interiors*, *163*(1-4), 83–105. Retrieved from https://doi.org/10.1016/j.pepi.2007.04.015

Hamiel, Y., Lyakhovsky, V., Stanchits, S., Dresen, G., & Ben-Zion, Y. (2009). Brittle deformation and damage-induced seismic wave anisotropy in rocks. *Geophysical Journal International*, *178*(2), 901–909. https://doi.org/10.1111/j.1365-246X.2009.04200.x

Hardebeck, J. L., & Hauksson, E. (1999). Role of fluids in faulting inferred from stress field signatures. *Science*, *285*(5425), 236–239. https://doi.org/10.1126/science.285.5425.236

Hardebeck, J. L., & Michael, A. J. (2004). Stress orientations at intermediate angles to the San Andreas Fault, California. *Journal of Geophysical Research*, *109*, B11303. https://doi.org/10.1029/2004JB003239

Harris, R. A. (2017). Large earthquakes and creeping faults. *Reviews of Geophysics*, *55*, 169–198. https://doi.org/10.1002/2016RG000539

Heidbach, O., Rajabi, M., Cui, X., Fuchs, K., Müller, B., Reinecker, J., et al. (2018). The world stress map database release 2016: Crustal stress pattern across scales. *Tectonophysics*, *744*(July), 484–498. Retrieved from https://doi.org/10.1016/j.tecto.2018.07.007

Herrendörfer, R. (2018). Modeling of the slip spectrum along mature and spontaneously forming faults in a visco-elasto-plastic continuum (Doctoral dissertation), ETH Zurich. https://doi.org/10.3929/ethz-b-000304601

Herrendörfer, R., Gerya, T. V., & van Dinther, Y. (2018). An invariant rate- and state-dependent friction formulation for viscoeastoplastic earthquake cycle simulations. *Journal of Geophysical Research: Solid Earth*, *123*, 5018–5051. https://doi.org/10.1029/2017JB015225

Hickman, S., & Zoback, M. (2004). Stress orientations and magnitudes in the SAFOD pilot hole. *Geophysical Research Letters*, *31*, L15S12. https://doi.org/10.1029/2004GL020043

Hirsch, P. B. (1975). Work hardening. In P. B. Hirsch (Ed.), *The physics of metals 2. Defects*. Cambridge: Cambridge University Press.

Ida, Y. (1974). Slow-moving deformation pulses along tectonic faults. *Physics of the Earth and Planetary Interiors*, *9*(4), 328–337. https://doi.org/10.1016/0031-9201(74)90060-0

Jolivet, R., Lasserre, C., Doin, M.-P., Peltzer, G., Avouac, J.-P., Sun, J., & Dailu, R. (2013). Spatio-temporal evolution of aseismic slip along the Haiyuan fault, China: Implications for fault frictional properties. *Earth and Planetary Science Letters*, *377-378*, 23–33. Retrieved from https://doi.org/10.1016/j.epsl.2013.07.020

Kame, N., Rice, J. R., & Dmowska, R. (2003). Effects of prestress state and rupture velocity on dynamic fault branching. *Journal of Geophysical Research*, *108*(B5), 2265. Retrieved from https://doi.org/10.1029/2002JB002189

Kame, N., & Yamashita, T. (1999). Simulation of the spontaneous growth of a dynamic crack without constraints on the crack tip path. *Geophysical Journal International*, *139*(2), 345–358. Retrieved from https://doi.org/10.1046/j.1365-246x.1999.00940.x

Kame, N., & Yamashita, T. (2003). Dynamic branching, arresting of rupture and the seismic wave radiation in self-chosen crack path modelling. *Geophysical Journal International*, *155*(3), 1042–1050. Retrieved from https://doi.org/10.1111/j.1365-246X.2003.02113.x

Kaus, B. J. P. (2010). Factors that control the angle of shear bands in geodynamic numerical models of brittle deformation. *Tectonophysics*, *484*(1-4), 36–47. Retrieved from https://doi.org/10.1016/j.tecto.2009.08.042

King, Y. C., Nason, R. D., & Tocher, D. (1973). Kinematics of fault creep. *Philosophical Transactions of the Royal Society. Series A, Mathematical and Physical Sciences*, *274*(1239), 355–360.

Kohlstedt, D. L., Evans, B., & Mackwell, S. J. (1995). Strength of the lithosphere: Constraints imposed by laboratory experiments. *Journal of the Franklin Institute*, *181*(6), 845–848. https://doi.org/10.1016/S0016-0032(16)90156-X

Lapusta, N., & Barbot, S. (2012). Models of earthquakes and aseismic slip based on laboratory-derived rate and state friction laws. In A. Bizzarri & H. S. Bhat (Eds.), *The mechanics of Faulting: From Laboratory to Real Earthquakes* (Vol. 661). Kerala, India: Research Signpost.

Lapusta, N., & Liu, Y. (2009). Three-dimensional boundary integral modeling of spontaneous earthquake sequences and aseismic slip. *Journal of Geophysical Research*, *114*, B09303. https://doi.org/10.1029/2008JB005934

Lapusta, N., Rice, J. R., Ben-Zion, Y., & Zheng, G. (2000). Elastodynamic analysis for slow tectonic loading with spontaneous rupture episodes on faults with rate- and state-dependent friction. *Journal of Geophysical Research*, *105*, 23,765–23,789. https://doi.org/10.1029/2000JB900250

Lavier, L. L., Buck, W. R., & Poliakov, A. N. B. (2000). Factors controlling normal fault offset in an ideal brittle layer. *Journal of Geophysical Research*, *105*(B10), 23,431–23,442. Retrieved from https://doi.org/10.1029/2000JB900108

Lehner, F. K., Li, V. C., & Rice, J. R. (1981). Stress diffusion along rupturing plate boundaries. *Journal of Geophysical Research*, *86*, 6155–6169.

Li, Z., Peng, Z., Ben-Zion, Y., & Vernon, F. L. (2015). Spatial variations of shear wave anisotropy near the San Jacinto fault zone in Southern California. *Journal of Geophysical Research: Solid Earth*, *120*, 8334–8347. https://doi.org/10.1002/2015JB012483

Lindsey, E. O., Fialko, Y., Bock, Y., Sandwell, D. T., & Bilham, R. (2014). Localized and distributed creep along the southern San Andreas Fault. *Journal of Geophysical Research: Solid Earth*, *119*, 7909–7922. https://doi.org/10.1002/2014JB011275

Liu, F., & Borja, R. I. (2008). A contact algorithm for frictional crack propagation with the extended finite element method. *International Journal for Numerical methods in Engineering*, *76*(June), 1489–1512. https://doi.org/10.1002/nme

Liu, Y., & Rice, J. R. (2007). Spontaneous and triggered aseismic deformation transients in a subduction fault model. *Journal of Geophysical Research*, *112*, B09404. https://doi.org/10.1029/2007JB004930

Ma, X., & Elbanna, A. (2018). Strain localization in dry sheared granular materials: A compactivity-based approach. *Physical Review E*, *98*(2), 022906. Retrieved from https://doi.org/10.1103/PhysRevE.98.022906

Manighetti, I., Campillo, M., Sammis, C., Mai, P. M., & King, G. (2005). Evidence for self-similar, triangular slip distributions on earthquakes: Implications for earthquake and fault mechanics. *Journal of Geophysical Research*, *110*, B05302. https://doi.org/10.1029/2004JB003174

Manighetti, I., King, G. C. P., Gaudemer, Y., Scholz, C. H., & Doubre, C. (2001). Slip accumulation and lateral propagation of active normal faults in Afar. *Journal of Geophysical Research*, *106*(B7), 13,667–13,696.

Manighetti, I., King, G., & Sammis, C. G. (2004). The role of off-fault damage in the evolution of normal faults. *Earth and Planetary Science Letters*, *217*(3-4), 399–408. https://doi.org/10.1016/S0012-821X(03)00601-0

Manning, C. E., & Ingebritsen, S. E. (1999). Permeability implications of the continental of geothermal data crust and metamorphic systems. *Reviews of Geophysics*, *37*(1), 127–150.

Manning, M. L., Langer, J. S., & Carlson, J. M. (2007). Strain localization in a shear transformation zone model for amorphous solids. *Physical Review E - Statistical, Nonlinear, and Soft Matter Physics*, *76*(5), 056106. https://doi.org/10.1103/PhysRevE.76.056106

Meyer, S. E., Kaus, B., & Passchier, C. (2017). Development of branching brittle and ductile shear zones: A numerical study. *Geochemistry, Geophysics, Geosystems*, *18*, 2054–2075. Retrieved from https://doi.org/10.1002/2016GC006793

Misra, S., Ellis, S., & Mandal, N. (2015). Fault damage zones in mechanically layered rocks: The effects of planar anisotropy. *Journal of Geophysical Research: Solid Earth*, *120*, 5432–5452. https://doi.org/10.1002/2014JB011780

Mitchell, T. M., & Faulkner, D. R. (2009). The nature and origin of off-fault damage surrounding strike-slip fault zones with a wide range of displacements: A field study from the Atacama fault system, northern Chile. *Journal of Structural Geology*, *31*(8), 802–816. https://doi.org/10.1016/j.jsg.2009.05.002

Nakatani, M. (2001). Conceptual and physical clarification of rate and state friction: Frictional sliding as a thermally activated rheology. *Journal of Geophysical Research*, *106*(B7), 13,347–13,380. https://doi.org/10.1029/2000jb900453

Nasseri, M. H., Rezanezhad, F., & Young, R. P. (2010). Analysis of fracture damage zone in anisotropic granitic rock using 3D X-ray CT scanning techniques. *International Journal of Fracture*, *168*(1), 1–13. https://doi.org/10.1007/s10704-010-9551-0

Noda, H., & Lapusta, N. (2013). Stable creeping fault segments can become destructive as a result of dynamic weakening. *Nature*, *493*(7433), 518–521. Retrieved from https://doi.org/10.1038/nature11703

Norris, R. J., & Toy, V. G. (2014). Continental transforms: A view from the Alpine Fault. *Journal of Structural Geology*, *64*, 3–31. Retrieved from https://doi.org/10.1016/j.jsg.2014.03.003

Nur, A., Ron, H., & Beroza, G. (1993). Landers-Mojave earthquake line: A new fault system?(Vol. 3) (No. 10).

Nur, A., Ron, H., & Scottti, O. (1989). Kinematics and mechanics of tectonic block rotations. *Geophysical*, *49*, 31–46.

Oppenheimer, D. H., Bakun, W. H., & Lindh, A. G. (1990). Slip partitioning of the Calaveras Fault, California, and prospects for future earthquakes. *Journal of Geophysical Research*, *95*(90), 8483–8498.

Peacock, D. C. (1991). Displacements and segment linkage in strike-slip fault zones. *Journal of Structural Geology*, *13*(9), 1025–1035. https://doi.org/10.1016/0191-8141(91)90054-M

Peacock, D. C., & Sanderson, D. J. (1992). Effects of layering and anisotropy on fault geometry. *Journal of the Geological Society*, *149*(5), 793–802. https://doi.org/10.1144/gsjgs.149.5.0793

Peacock, D. C., & Sanderson, D. J. (1996). Effects of propagation rate on displacement variations along faults. *Journal of Structural Geology*, *18*(2-3), 311–320. https://doi.org/10.1016/S0191-8141(96)80052-6

Perrin, C., Manighetti, I., Ampuero, J.-P., Cappa, F., & Gaudemer, Y. (2016). Location of largest earthquake slip and fast rupture controlled by along-strike change in fault structural maturity due to fault growth. *Journal of Geophysical Research: Solid Earth*, *121*, 3666–3685. https://doi.org/10.1002/2015JB012671

Perrin, C., Manighetti, I., & Gaudemer, Y. (2016). Off-fault tip splay net works: A genetic and generic property of faults indicative of their longterm propagation. *Comptes Rendus - Geoscience*, *348*(1), 52–60. https://doi.org/10.1016/j.crte.2015.05.002

Plesch, A., Nicholson, C., Shaw, J., Marshall, S., Su, M.-H., & Maechling, P. (2017). The SCEC community fault model (CFM). Retrieved from https://www.scec.org/research/cfm

Plesch, A., Shaw, J. H., Benson, C., Bryant, W. A., Carena, S., Cooke, M., et al. (2007). Community fault model (CFM) for southern California. *Bulletin of the Seismological Society of America*, *97*(6), 1793–1802. https://doi.org/10.1785/0120050211

Poliakov, A. N. B., Dmowska, R., & Rice, J. R. (2002). Dynamic shear rupture interactions with fault bends and off-axis secondary faulting. *Journal of Geophysical Research*, *107*(B11), 2295. https://doi.org/10.1029/2001JB000572

Preuss, S., Herrendörfer, R., Gerya, T., Ampuero, J., & van Dinther, Y. (2019). Model data set and video to "Seismic and aseismic fault growth lead to different fault orientations". https://doi.org/10.3929/ethz-b-000307985

Rawling, G. C., Baud, P., & Wong, T.-f (2002). Dilatancy, brittle strength, and anisotropy of foliated rocks: Experimental deformation and micromechanical modeling. *Journal of Geophysical Research*, *107*(B10), 2234. https://doi.org/10.1029/2001jb000472

Regenauer-Lieb, K., Hobbs, B., Yuen, D. A., Ord, A., Zhang, Y., Mulhaus, H. B., & Morra, G. (2006). From point defects to plate tectonic faults. *Philosophical Magazine*, *86*(21-22), 3373–3392. https://doi.org/10.1080/14786430500375159

Regenauer-Lieb, K., & Yuen, D. A. (2003). Modeling shear zones in geological and planetary sciences: Solid- and fluid-thermal-mechanical approaches. *Earth-Science Reviews*, *63*(3-4), 295–349. https://doi.org/10.1016/S0012-8252(03)00038-2

Rice, J. R. (1980). The mechanics of earthquake rupture. In A. M. Dziewonski & E. Boschi (Eds.), *Physics of the Earth's Interior* (78th ed., pp. 555–649). https://doi.org/10.1.1.161.3251

Rice, J. R. (1993). Spatio-temporal complexity of slip on a fault. *Journal of Geophysical Research*, *98*(B6), 9885–9907. https://doi.org/10.1029/93JB00191

Rockwell, T. K., Lindvall, S., Herzberg, M., Murbach, D., Dawson, T., & Berger, G. (2000). Paleoseismology of the Johnson Valley, Kickapoo, and Homestead Valley faults: Clustering of earthquakes in the Eastern California shear zone. *Bulletin of the Seismological Society of America*, *90*(5), 1200–1236. https://doi.org/10.1785/0119990023

Ron, H., Freund, R., Garfunkel, Z., & Nur, A. (1981). Block rotation by strike-slip faulting: Structural and paleomagnetic evidence. *Journal of Geophysical Research*, *89*(B7), 6256–6270. https://doi.org/10.1029/JB089iB07p06256

Ross, Z. E., Hauksson, E., & Ben-Zion, Y. (2017). Abundant off-fault seismicity and orthogonal structures in the San Jacinto fault zone. *Science Advances*, *3*, e1601946.

Roubíček, T. (2014). A note about the rate-and-state-dependent friction model in a thermodynamic framework of the Biot-type equation. *Geophysical Journal International*, *199*(1), 286–295. https://doi.org/10.1093/gji/ggu248

Rubin, A. M., & Ampuero, J. P. (2005). Earthquake nucleation on (aging) rate and state faults. *Journal of Geophysical Research*, *110*, B11312. https://doi.org/10.1029/2005JB003686

Ruina, A. (1983). Slip instability and state variable friction laws. *Journal of Geophysical Research*, *88*(B12), 10,359–10,370. https://doi.org/10.1029/JB088iB12p10359

Schaff, D. P., & Beroza, G. C. (2004). Coseismic and postseismic velocity changes measured by repeating earthquakes. *Journal of Geophysical Research*, *109*, B10302. https://doi.org/10.1029/2004JB003011

Scholz, C. H., Ando, R., & Shaw, B. E. (2010). The mechanics of first order splay faulting: The strike-slip case. *Journal of Structural Geology*, *32*(1), 118–126. Retrieved from https://doi.org/10.1016/j.jsg.2009.10.007

Scholz, C. H., & Lawler, T. M. (2004). Slip tapers at the tips of faults and earthquake ruptures. *Geophysical Research Letters*, *31*, L21609. https://doi.org/10.1029/2004GL021030

Segall, P., & Pollard, D. D. (1980). Mechanics of discontinuous faults. *Journal of Geophysical Research*, *85*(B8), 4337–4350. https://doi.org/10.1029/JB085iB08p04337

Segall, P., & Pollard, D. D. (1983). Nucleation and growth of strike slip patterns in Granite. *Journal of Geophysical Research*, *88*(2), 555–568.

Şengör, A., Tüysüz, O., Imren, C., Sakınç, M., Eyidogan, H., Görür, N., et al. (2004). The North Anatolian fault: A new look. *Annual Review of Earth and Planetary Sciences*, *33*(1), 37–112. https://doi.org/10.1146/annurev.earth.32.101802.120415

Sibson, R. H. (1990). Rupture nucleation on unfavorably oriented faults. *Bulletin of the Seismological Society of America*, *80*(6), 1580–1604. Retrieved from https://doi.org/10.1021/jp111520r

Sibson, R. H. (1994). An assessment of field evidence for 'Byerlee' friction. *Pure and Applied Geophysics PAGEOPH*, *142*(3-4), 645–662. https://doi.org/10.1007/BF00876058

Sibson, R., Ghisetti, F., & Ristau, J. (2011). Stress control of an evolving strike-slip fault system during the 2010–2011 Canterbury, New Zealand, earthquake sequence. *Seismological Research Letters*, *82*(6), 824–832. Retrieved from https://doi.org/10.1785/gssrl.82.6.824

Sibson, R. H., & Rowland, J. V. (2003). Stress, fluid pressure and structural permeability in seismogenic crust, North Island, New Zealand. *Geophysical Journal International*, *154*(2), 584–594. Retrieved from https://doi.org/10.1046/j.1365-246X.2003.01965.x

Sieh, K., Hauksson, E., Hutton, K., Kanamori, H., Lilje, A., Spotila, J. A., et al. (1993). Near-field investigations of the Landers earthquake sequence, April to July 1992. *Science*, *260*(5105), 171–176. https://doi.org/10.1126/science.260.5105.171

Sleep, N. H., Richardson, E., & Marone, C. (2000). Physics of friction and strain rate localization in synthetic fault gouge. *Journal of Geophysical Research*, *105*(B11), 25,875–25,890. Retrieved from https://doi.org/10.1029/2000JB900288

Socquet, A., Valdes, J. P., Jara, J., Cotton, F., Walpersdorf, A., Cotte, N., et al. (2017). An 8 month slow slip event triggers progressive nucleation of the 2014 Chile megathrust. *Geophysical Research Letters*, *44*, 4046–4053. https://doi.org/10.1002/2017GL073023

Stein, R. S., King, G. C. P., & Lin, J. (1992). Change in failure stress on the southern San Andreas fault system caused by the 1992 magnitude = 7.4 Landers earthquake. *Science*, *258*(5086), 1328–1332.

Tarasewicz, J. P., Woodcock, N. H., & Dickson, J. A. D. (2005). Carbonate dilation breccias: Examples from the damage zone to the Dent Fault, northwest England. *Bulletin of the Geological Society of America*, *117*(5-6), 736–745. https://doi.org/10.1130/B25568.1

Townend, J., & Zoback, M. D. (2004). Regional tectonic stress near the San Andreas fault in central and southern California. *Geophysical Research Letters*, *31*, L15S11. https://doi.org/10.1029/2003GL018918

van Dinther, Y., Gerya, T., Dalguer, L. A., Corbi, F., Funiciello, F., & Mai, P. M. (2013). The seismic cycle at subduction thrusts: 2. Dynamic implications of geodynamic simulations validated with laboratory models. *Journal of Geophysical Research: Solid Earth*, *118*, 1502–1525. https://doi.org/10.1029/2012JB009479

van Dinther, Y., Gerya, T., Dalguer, L. A., Mai, P. M., Morra, G., & Giardini, D. (2013). The seismic cycle at subduction thrusts: Insights from seismo-thermomechanical models. *Journal of Geophysical Research: Solid Earth*, *118*, 6183–6202. https://doi.org/10.1002/2013JB010380

van Dinther, Y., Mai, P. M., Dalguer, L. A., & Gerya, T. (2014). Modeling the seismic cycle in subduction zones: The role and spatiotemporl occurrence of off-megathrust earthquakes. *Geophysical Research Letters*, *41*, 1194–1201. https://doi.org/10.1002/2013GL058886

Veedu, D. M., & Barbot, S. (2016). The Parkfield tremors reveal slow and fast ruptures on the same asperity. *Nature*, *532*(7599), 361–365. https://doi.org/10.1038/nature17190

Vermeer, P. A. (1990). The orientation of shear bands in biaxial tests. *Géotechnique*, *40*(2), 223–236. Retrieved from https://doi.org/10.1680/geot.1990.40.2.223

Weng, H., & Yang, H. (2017). Seismogenic width controls aspect ratios of earthquake ruptures. *Geophysical Research Letters*, *44*, 2725–2732. https://doi.org/10.1002/2016GL072168

Willemse, E. J. M., & Pollard, D. D. (1998). On the orientation and patterns of wing cracks and solution surfaces at the tips of a sliding flaw or fault. *Journal of Geophysical Research*, *103*(B2), 2427–2438. https://doi.org/10.1029/97JB01587

Woodcock, N. H., Dickson, J. A. D., & Tarasewicz, J. P. T. (2007). Transient permeability and reseal hardening in fault zones: Evidence from dilation breccia textures. *Geological Society, London, Special Publications*, *270*(1), 43–53. https://doi.org/10.1144/gsl.sp.2007.270.01.03

Xu, S., & Ben-Zion, Y. (2013). Numerical and theoretical analyses of in-plane dynamic rupture on a frictional interface and off-fault yielding patterns at different scale. *Geophysical Journal International*, *193*(1), 304–320. https://doi.org/10.1093/gji/ggs105

Zang, A., & Stephansson, O. (2010). *Stress field of the Earth's crust*. Dordrecht: Springer Netherlands. Retrieved from https://doi.org/10.1007/978-1-4020-8444-7

Zoback, M. D. (1991). State of stress and crustal deformation along weak transform faults. *Philosophical Transactions - Royal Society of London, A*, *337*(1645), 141–150. https://doi.org/10.1098/rsta.1991.0112

Zoback, M., Hickman, S., & Ellsworth, W. (2010). Scientific drilling into the San Andreas fault zone. *Eos, Transactions American Geophysical Union*, *91*(22), 197–204. Retrieved from http://www.agu.org/pubs/eos-news/supplements/2010/zoback_91_22.shtml

Zoback, M. D., Zoback, M. L., Mount, V. S., Suppe, J., Eaton, J. P., Healy, J. H., et al. (1987). New evidence on the state of stress of the San Andreas fault system. *Science*, *238*(4830), 1105–1111.